Keratin 16 spatially inhibits type I interferon responses in stressed skin

Erez Cohen[1], Yang Xu[2], Amanda Orosco[1], Dajia Wang[1], Craig N. Johnson[1], Kaylee Steen[1], Mrinal K. Sarkar[3], Nurhan Özlü[4], Lam C Tsoi[3], Johann E. Gudjonsson[3], Carole A. Parent[1,2,5,6] and Pierre A. Coulombe[1,3,6,#]

[1] Department of Cell & Developmental Biology, University of Michigan Medical School, Ann Arbor, MI;

[2] Department of Pharmacology, University of Michigan Medical School, Ann Arbor, MI;

[3] Department of Dermatology, University of Michigan Medical School, Ann Arbor, MI;

[4] Department of Molecular Biology and Genetics, Science Faculty, Koç University, Istanbul, Turkey ;

[5] Life Sciences Institute, University of Michigan, Ann Arbor, MI, ;

[6] Rogel Cancer Center, University of Michigan, Ann Arbor, MI.

[#] Corresponding author. Address: Pierre A. Coulombe, Ph.D., Dept. of Cell & Developmental Biology, University of Michigan Medical School, 109 Zina Pitcher Place, Ann Arbor, MI 48109, USA. E-mail: coulombe@umich.edu ; Tel: 734-615-7509.

Short title: Keratin 16 inhibits type I interferon signaling in skin.

Key words: skin, stratified epithelia, epidermis, keratinocyte, keratin, intermediate filament, homeostasis, differentiation, stress response, inflammation, innate immunity, type I interferon signaling, single cell biology, RNAseq.

None of the authors have a conflict of interest to declare.

Abstract

The stress-induced keratin intermediate filament gene/protein *KRT16* (K16) is spatially restricted to the suprabasal compartment of the epidermis and extensively used as a biomarker for psoriasis, hidradenitis suppurativa, atopic dermatitis and other inflammatory disorders. However, its role in these conditions remains poorly defined. Here we show that K16 negatively regulates type-I interferon (IFN) signaling and innate immune responses. In mouse skin *in vivo,* loss of *Krt16* leads to exacerbation of imiquimod-induced psoriasiform disease and heightened recruitment of neutrophils in a phorbol ester-induced model of acute sterile inflammation. In *KRT16* null human keratinocytes, loss of K16 amplifies IFN signaling including phospho-IRF7 and ISG15 after treatment with synthetic dsRNA poly(I:C). Mechanistically, K16 interacts with effectors of the RIG-I-like receptor (RLR) pathway, including 14-3-3ε, and inhibits the 14-3-3ε:RIG-I interaction upstream of IFN activation *in vivo* and *ex vivo*. These findings uncover a new paradigm for keratin-dependent regulation of innate immunity, with significant implications for our understanding of inflammatory skin diseases.

Introduction

Keratinocytes in the interfollicular epidermis constantly encounter environmental, mechanical, and pathological insults. Disruption of keratinocyte homeostasis is linked to many inflammatory diseases, including psoriasis (PSOR), hidradenitis suppurativa (HS), atopic dermatitis, and pachyonychia congenita (PC) (Gallegos-Alcalá et al., 2021; Leachman et al., 2005; Nguyen et al., 2021; Rendon and Schäkel, 2019; Zieman and Coulombe, 2020). Over the past decade, research on inflammatory skin diseases has underscored how the interaction between the epidermis and the immune system, known as epithelial-immune crosstalk, is a key determinant for disease onset (Pasparakis et al., 2014). This communication involves complex interactions between keratinocytes, their niche, and both innate and adaptive immunity (Rosenblum and Naik, 2022), and is highly dynamic and tightly regulated. Its failure can disrupt the epithelial barrier (Rosenblum and Naik, 2022), while a hyperactive response can trigger inflammatory diseases, such as in the Koebner phenomenon, where keratinocytes stress triggers the resurgence of psoriatic lesions (Weiss et al., 2002). Understanding how keratinocytes manage this crosstalk and recruit innate immune cells, the first immune responders to stress, is critical for the treatment of inflammatory skin diseases.

Keratin intermediate filaments are among the most abundant proteins in skin keratinocytes (Cohen et al., 2022; Feng et al., 2012; Moll et al., 2008; Sun and Green, 1978) and were recently identified to play a role in the recruitment of neutrophils to stress-responsive interfollicular epidermis (Xu et al., 2024b). Traditionally, keratins have been known to maintain cellular structural integrity in response to various stresses (Fuchs and Cleveland, 1998; Omary et al., 2004). However, recent studies have highlighted their role in regulating cellular signaling including immune response, DNA damage, oxidative stress, and cell growth and differentiation (Guo et al., 2020; Hobbs et al., 2012; Kerns et al., 2016; Kim et al., 2006; Nair et al., 2021). It has been suggested that protein-protein interactions are central to keratin function in cellular signaling, with a reliance on post-translational modifications for regulation (Di Russo et al., 2023; Li et al., 2023; Pallari and Eriksson, 2006). Among the 54 functional keratin genes, three particularly stand out as stress-responsive in skin and other complex epithelia: the type I keratins 16 and 17 (K16,

K17) and type II keratin 6 paralogs (K6A/B/C). These stress-responsive keratins serve as biomarkers for PSOR (Jiang et al., 2015; Rashmi et al., 2009) and many additional chronic skin inflammatory disorders, with expression linked to pathways mediating innate immunity (Cohen et al., 2024). Mutations in any one of these five keratin genes cause PC, a debilitating skin disease related to ectodermal dysplasia (Leachman et al., 2005; McLean et al., 1995) However, the cellular mechanism and signaling pathways underlying these functions, and the precise significance of these keratins to the onset and development of inflammatory skin diseases, remains underexplored.

Here, we examined the role of K16 in the context of psoriasiform disease and recruitment of innate immunity. K16 is not expressed in healthy epidermis (with the notable exception of palm and sole skin) but is rapidly induced in differentiating keratinocytes of epidermis experiencing various stresses, and is commonly used as a biomarker of PSOR and other chronic inflammatory disorders. *Krt16* null mice exhibit aberrant differentiation and oxidative stress responses (Kerns et al., 2016; Zieman et al., 2019) along with increased recruitment of innate immune cells upon chemical irritation (Lessard et al., 2013). Analyses of high-throughput proteomics and transcriptomics datasets uncovered interactions between K16 and members of Type-I Interferon (IFN) pathway, known for its involvement in the onset of PSOR and, specifically, the Koebner phenomenon (Zhang, 2019; Zhang et al., 2023). Using *Krt16* null mice, we identified K16 as a negative regulator of imiquimod-induced psoriasiform disease and of the recruitment of innate immune cells to sites of repeated stress. Utilizing an immortalized human N/TERT keratinocyte cell line (Dickson et al., 2000), we identified that K16 acts upstream of the IFN pathway activation and limits the interactions between 14-3-3ε and RIG-I, a member of the RLR sensors of dsRNA and LL-37 (Zhang et al., 2016). These observations provide insights into the significance of K16 in the context of inflammatory diseases of the skin and define a novel role for K16 in the regulation of RIG-I-like Receptor (RLR) and type-I IFN signaling.

Results

K16 expression is limited to the suprabasal interfollicular epidermis and inversely related to expression of Type-I IFN response genes in human disease and mouse models

To explore the potential signaling pathways interacting with K16 in inflammatory diseases, we examined differentially expressed genes in cells with high versus low levels of *KRT16* transcripts using single-cell RNAseq data collected from the skin of PSOR and HS patients (Cohen et al., 2024). These analyses revealed a significant downregulation of IFN signaling genes in *KRT16*^{high} expressing cells **(Fig. 1A).** We next examined the spatial relationship between *KRT16* transcripts and those of differentially responsive IFN genes *IFITM3*, *IFITM1*, and *CD74* in spatial single-cell datasets from PSOR and HS lesions. These analyses showed that *KRT16* is strongly expressed in the suprabasal layers in the epidermis of lesional skin (**Fig. S1A-A', B-B')**, consistent with immunofluorescence staining for K16 protein **(Fig. 1B-C)** and contrasting with the pattern of K14 and K5 protein **(Fig. S1C-D).** Analysis of spatial single-cell sequencing further shows that the IFN responsive genes *IFITM1*, *IFITM3* and *CD74* are spatially restricted to the basal layer (**Fig. S1A-B"**)**.** To further explore this connection, we screened for K16 interacting proteins by transfecting HaCaT keratinocytes (Boelsma et al., 1999) with 3xFLAG-K16 or empty-vector (EV) and performing co-immunoprecipitation, using FLAG antibodies, followed by mass spectrometry **(Fig. 1D)**. In addition to other keratins including K16's type II keratin partner K6, several IFN response proteins occurred in the filtered list of hits (SAINT>0.8), including RIG-I (DDX58) and MDA5 (IFIH1) members of the RLR (RIG-I-like receptors) family (Zhang et al., 2016) (**Fig. 1D-F)**. To further explore the relationship between *KRT16* and IFN signaling, we examined publicly available microarray (bulk) transcriptomic data from individuals with PC (Cao et al., 2015), a rare genetic disorder caused by mutations in the stress-responsive keratins *KRT6A-C*, *KRT16* and *KRT17*. Specifically, we analyzed data from 6 patients with *KRT16* or *KRT6A-B* mutations (n=3 each; Cao et al., 2015). The effort yielded a significant enrichment for genes involved in type I IFN responses (**Fig. 1G**). Similarly, analysis of pathways enriched in the PC-like palmoplantar keratoderma lesions in the footpad skin of *Krt16* null mice,

subjected to microarray analysis (Zieman et al., 2019), showed a differential expression of IFN response genes (**Fig. 1H)**. Together, these observations support the association between K16 and the IFN signaling pathway across inflammatory diseases, model animals and *ex vivo* cell culture models.

Loss of *Krt16* leads to exacerbated psoriasiform disease in imiquimod-treated mice

To test whether K16 plays a role in the development of psoriasiform disease, we assessed the response of *Krt16* null mouse skin to imiquimod (IMQ) cream (Aldara™), a widely recognized model of psoriasiform disease (Van Der Fits et al., 2009). *Krt16* null mice and wildtype (WT) littermates (FVB strain) were shaved and topically treated for 5 consecutive days with Aldara™ cream or Vaseline control as previously established **(Fig. 2A**; (Van Der Fits et al., 2009, see Methods)**.** Treated mice were assessed daily **(Fig. 2B-E)**. At baseline, *Krt16* null and WT shaved back skin did not show any visually noticeable differences in erythema or scaling, with no difference in thickness or scaling perceptible by touch **(Fig. 2B,D)**. *Krt16* null mice began exhibiting onset of psoriasiform disease as early as day 2 of the 5-day IMQ treatment regimen (**Fig. S2A,B)**, and by day 4, a clear exacerbation of disease with increased erythema and scaling, relative to controls and WT littermates, was evident **(Fig. 2C,E; Fig. S2G-J).** During tissue harvesting (day 5) we noted an increase in vasculature in IMQ-treated *Krt16* null skin relative to untreated back skin within the same mice (**Fig. S2C-F)**, suggesting that the response is restricted to the treated area. Day 5 skin samples were processed for histological analyses. Both hematoxylin and eosin staining (**Fig. 2F-I)** and indirect immunofluorescence staining (**Fig. 2J-M)** showed increased acanthosis in IMQ-treated *Krt16* null skin compared to IMQ-treated WT controls. As expected, a robust K16 induction was observed in IMQ-treated WT skin but not in controls or *Krt16* null mice **(Fig. 2J-L)**. We also observed an expansion of K14 immunostaining across the suprabasal layers, indicative of aberrant differentiation (Cohen et al., 2024), as previously reported for both the IMQ model in mouse and PSOR patients (Walter et al., 2013; and **Fig. S1D)**. We then tested whether loss of K16 in the IMQ paradigm leads to changes in cellular proliferation. We previously showed that K16 induction in inflammatory diseases is not associated with mitosis at the single-cell level. Instead, the association of K16 with hyperproliferation is non-cell autonomous and takes

place at the tissue level (Cohen et al., 2024). Loss of *Krt16* resulted in an increased mitotic index as observed by Ki67 staining **(Fig. 2N-Q).** This increase occurs in both basal and suprabasal layers of the acanthotic epidermis, consistent with the occurrence of aberrant differentiation **(Fig. S2K-K")** and previous data from PSOR skin (Sezer et al., 2015). Lastly, we tested whether K16 expression negatively correlates with IFN response genes in the IMQ treatment model. To do so, we stained for OAS1, a robust IFN-responsive gene, which is elevated in human PSOR skin (**Fig. S1A"'** and Huang et al., 2022), psoriasiform disease models (Dickson et al., 2015; Swindell et al., 2017) and during acute sterile inflammation in mouse skin (Xu et al., 2024b). In line with our analysis of IFN responsive genes in PSOR and HS patients **(Fig. S1A-B")**, OAS1 staining was increased in IMQ-treated mice compared to controls (**Fig. 2R-S', Fig. S2L-M).** Importantly, in IMQ-treated WT mice, we noted a clear difference between OAS1 staining in the basal and suprabasal layer of the epidermis, with the basal layer showing higher levels of staining **(Fig. 2R-R',T)**. In stark contrast, we did not detect a difference in OAS1 staining between the layers of epidermis in *Krt16* null mice **(Fig. 2S-T)**, suggesting that K16 participates in restricting the IFN response to the basal layer in stress response and psoriasiform disease.

Loss of K16 leads to amplified recruitment of neutrophils in a phorbol ester-induced model of acute inflammation

Topical tetradecanoylphorbol-13 acetate (TPA) treatment provides an acute and sterile inflammation model that allows for an assessment of the kinetics and dynamics of neutrophil recruitment to the site of treatment in mouse skin, thus complementing the IMQ model. Repeated topical application of TPA results in a Transiently Amplified neutrophil inflammation Response (TAR) in mouse ear skin, which is partially dependent on K17 (Xu et al., 2024b) and is associated with IFN-responsive genes *OAS1, IFITM1 and IFI16*. We topically applied TPA or Acetone (vehicle control) to mouse ear epidermis of *Krt16* null or WT littermates. We then assessed neutrophil recruitment (Ly6g staining) 6h after a single TPA treatment, or 6h after dual treatment, with the latter showing the characteristic TAR signature **(Fig. 3A-E)**. As we previously showed (Xu et al., 2024b), WT mice showed a modest increase in Ly6g staining 6h after a single TPA treatment, and a markedly

accelerated and amplified response at 6h after a second TPA treatment **(Fig. 3B,D)**. By contrast, we observed a significant increase in neutrophil influx in TPA-treated *Krt16* null ear epidermis after both a single or dual TPA treatments **(Fig. 3C,E-G')**. Otherwise, TPA treatment led to significantly more edema in *Krt16* null relative to WT skin (cartilage to dorsal, **Fig. 3G').**

We next tested whether the loss of *Krt16 in vivo* leads to changes in basal-restricted IFN response genes in the TPA-induced TAR paradigm. Consistent with previous reports (Xu et al., 2024b), we observed increased OAS1 immunostaining in both WT (**Fig. 3H-J)** and *Krt16* null mouse **(Fig. 3K-L')** treated twice with TPA, 24h apart. Again, we noted that, in WT mice, the OAS1 induction was significantly higher in the basal relative to the suprabasal layers of treated epidermis **(Fig. 3I', M).** In striking similarity to the IMQ results, the differential restriction of OAS1 to the basal compartment was lost in *Krt16* null skin (**Fig. 3K-L')**. These findings further support a role for K16 in inhibiting IFN responses in the suprabasal layer and downstream recruitment of innate immune cells.

Loss of *KRT16* in human keratinocyte cells results in amplified responses to poly(I:C), increased recruitment of neutrophils and differentiation defects

To elucidate the molecular mechanism underlying the K16-mediated inhibition of immune recruitment and IFN signaling (**Fig. 4A**), we set out to identify an immortalized human cell line that recapitulates the spatial restriction of K16 expression during keratinocyte differentiation. To do so, we exploited the widely used N/TERT human keratinocyte cell line (Dickson et al., 2000). We adapted the N/TERT 3D culture protocol (Smits et al., 2017) to generate a post-confluent, uniformly bilayered epithelium in submerged culture under standard KSFM growth medium, without the need for 3D growth at liquid-air interface (see Methods*)*. Under such conditions, expression of keratinocyte differentiation markers including K10 and filaggrin is exclusive to the upper layer of keratinocytes (**Fig. S3A-C)**. Further, as is the case in epidermis in situ, we found that whole cell and nuclear size are expanded in the differentiated suprabasal layer of post-confluent N/TERT keratinocytes **(Fig. S3D)**. Importantly, K16 expression is restricted to, and uniform, in the suprabasal layer in this model (**Fig. S3A-B**). We generated and validated a *KRT16*

CRISPR KO N/TERT cell line using established methods (Sarkar et al., 2023) alongside mock sgRNA controls for the tubulin alpha pseudogene (see Methods and **Fig. 4B-C**).

Utilizing the differentiated, K16-expressing N/TERT model and the *KRT16* KO line, we tested the role of K16 in the induction of IFN signaling through synthetic dsRNA poly(I:C), known to activate the Type I IFN pathway in keratinocytes (Zhang et al., 2016) and relevant to the keratinocyte inflammatory response observed in PSOR and during the Koebner phenomenon (Zhang et al., 2016). Parental and *KRT16* KO keratinocytes were treated with poly(I:C) for 3h (short response) or 6h with 24h recovery (long response, or "recovery"), and immunostained for upstream regulators of IFN signaling across the RIG-I/MDA5/MAVS pathway (phosphorylated IRF3 and IRF7; (Seth et al., 2005), downstream effectors of TLR3 (p65 and phosphorylated p65 (Kawai and Akira, 2007), and the canonical IFN response factor ISG15 (Der et al., 1998; Perng and Lenschow, 2018). We found that poly(I:C) treatment leads to increases in phospho-IRF3 and phospho-p65 within 3h of treatment in both parental and *KRT16 KO* N/TERT cells (**Fig. 4B,D; Fig. S3E-G**)**.** Phosphorylation of these effectors was downregulated following a 24h recovery period, in both genotypes. This is in line with the rapid response expected for both IRF and p65, which is subject to post-translational modifications (Christian et al., 2016; Lin et al., 1998; Ning et al., 2011). Interestingly, we noted a modest yet significant increase in the level of phosphorylated IRF7 in the *KRT16* KO after 24h recovery from poly(I:C) treatment relative to either mock-treated or parental N/TERT cells **(Fig. 4B,D)**. We next assessed whether the IFN responsive ISG15 was amplified in *KRT16* KO cells. At baseline (no treatment), the *KRT16* KO and MOCK KO cell variants show reduced, but not significant, levels of ISG15 relative to parental N/TERT cells (fold change between WT vs KO=0.64 +/- 0.05 SE; WT vs Mock=0.53 +/-0.25 SE, P>0.1). Such a reduction in IFN signaling has been recently reported for all N/TERT CRISPR KO cell lines at baseline (Sarkar et al., 2023). After the 24h recovery from poly(I:C) treatment, however, we noted a strong induction of ISG15 levels **(Fig. 4B,E)**, particularly in the *KRT16 KO* cell line relative to parental and mock control cells. We further validated these findings using immunofluorescence for ISG15 (**Fig. 4F-J)** and pIRF7 **(Fig. 4K-O).** In line with our *in vivo* observations, therefore, these results establish that loss of *KRT16* leads to an

amplification of cellular responses to dsRNA in human keratinocytes *ex vivo*, and that this amplification is cell autonomous.

Finally, to bridge our *ex vivo* and *in vivo* observations, we tested whether the loss of K16 in N/TERT keratinocytes affects their ability to recruit neutrophils after either poly(I:C) or TPA treatments. To do so we assessed the ability of conditioned medium collected from treated N/TERT cell cultures to induce the migration of primary human neutrophils utilizing a transwell assay (**Fig. 4P**; see Methods). In response to either poly(I:C) or TPA, loss of K16 led to an amplified recruitment of neutrophils to the media (**Fig. 4Q-R**), further supporting a role for K16 in inhibiting the stress-responsive recruitment of key cellular effectors of innate immunity.

K16 interacts with 14-3-3ε, a direct regulator of RIG-I receptor activation

To identify the molecular mechanisms underlying the effect of K16 on the response to poly(I:C), we leveraged the endogenous expression of K16 in N/TERT keratinocytes post-confluence to identify K16-interacting proteins in immortalized, differentiated cells using IP/MS. This screen yielded a large number of 14-3-3 protein family members (by ranked order: sigma, theta, zeta/delta, epsilon, beta/alpha, gamma and eta; **Supplemental Table 1)**. Follow-up studies were focused on 14-3-3 epsilon(ε) due to its known involvement as an adaptor in RLR signaling and downstream IFN activation (Liu et al., 2012) and **Fig. 5A**). First, we tested whether loss of K16 impacts the level of 14-3-3ε. No significant change in 14-3-3ε levels could be detected in WT vs. *KRT16* KO cells, whether at baseline or after treatment with poly(I:C) in N/TERT cells **(Fig. 5B).** Using immunofluorescence, we observed colocalization between K16 filaments and 14-3-3ε in the K16-expressing suprabasal layer of post-confluent N/TERT cells (**Fig. 5C-D”).** To explore this interaction further, we performed proximity ligation assay (PLA) between K16 and 14-3-3ε in poly(I:C)-treated and untreated cells **(Fig. 5E-I)**. Analysis of the PLA signal included both *KRT16* KO cells and the K16-negative basal keratinocytes in parental cells. We measured a significant degree of spatial proximity between K16 and 14-3-3ε in the suprabasal layer of parental N/TERT cells (**Fig. 5J)**. The number of high-proximity signal was increased further following poly(I:C) treatment **(Fig. 5J)**. To further validate this interaction biochemically, we immunoprecipitated endogenous K16 and analyzed the resulting

eluates. Consistent with our IP/MS and PLA data, 14-3-3ε co-immunoprecipitated with K16 in both untreated and poly(I:C) treated N/TERT cells **(Fig. 5K)**.

We next used the 14-3-3pred software (Madeira et al., 2015) to analyze the K16 amino acid sequence for potential 14-3-3 binding sites. 14-3-3 proteins typically bind client proteins in a phosphorylation-dependent manner (Morrison, 2009) - this is the case for their previously reported binding to K18 (Liao and Omary, 1996), K19 (Mariani et al., 2020), and K17 (Kim et al., 2006) - a keratin highly homologous to K16. Interestingly, residue S44 in the N-terminal head domain of K16 (orthologous to S40 in mouse), which corresponds to the 14-3-3 binding site in K17 (Kim et al., 2006), was ranked as the highest predicted site for 14-3-3 interactions **(Fig. 5L)**. To assess whether K16 S40 phosphorylation occurs *in vivo*, we harvested ear skin from TPA-treated WT mice and used MS to map post-translational modifications across a time span of 0-48h after treatment **(Fig. 5M)**. This effort revealed a continuous increase in K16 protein levels following induction of TPA **(Fig. 5N)** along with increased phosphorylation at the K16 S40 site **(Fig. 5O)**. Together, these results establish that K16 binds 14-3-3ε in human keratinocytes *ex vivo* and suggest that the predicted binding site is phosphorylated following TPA application of mouse skin *in vivo.*

Loss of K16 increases 14-3-3:RIG-I interactions in treated keratinocytes *ex vivo* and in the IMQ model of psoriasiform disease *in vivo*

Our observation that K16 interacts with 14-3-3ε in N/TERT keratinocytes led us to hypothesize that K16 prevents the interaction of 14-3-3ε with RIG-I and the downstream activation of MAVS upstream of type I IFN signaling (Liu et al., 2012). We first stained N/TERT keratinocytes for RIG-I at baseline and following poly(I:C) treatment **(Fig. 6A-D)**. As expected, our data show increased RIG1 staining in poly(I:C)-treated cells in both parental and *KRT16* KO N/TERT cells. We then assessed spatial proximity between 14-3-3ε and RIG-I using PLA **(Fig. 6E-H)**. We observed an increased 14-3-3ε:RIG-I PLA signal following poly(I:C) treatment in WT keratinocytes (**Fig. 6E-F**), consistent with the known regulation of RIG-I/MAVS pathway via interactions with 14-3-3ε (Liu et al., 2012)**.** Furthermore, we observed an increase in PLA signal in *KRT16* KO keratinocytes relative

to parental in both untreated and poly(I:C) treated conditions, suggesting that loss of K16 primes cells towards a heightened response to this treatment **(Fig. 6G-H,M).**

We then tested whether this interaction is impacted by the K16 expression status *in vivo* in the IMQ psoriasiform disease model. While IMQ is a TLR7/TLR8 agonist and does not directly activate cytosolic RIG-I, recent studies reported on increased levels of RIG-I in keratinocytes after IMQ treatment , and identified a mechanistic role for RIG-I in the IMQ-induced production of IL23 by dendritic cells (Zhu et al., 2017). We conducted PLA assays for RIG-I and 14-3-3 in IMQ-treated WT and *Krt16* null mouse skin tissue sections. We found that the PLA signal between RIG1:14-3-3 is increased in the epidermis of *Krt16* null mice, indicating increased spatial proximity relative to controls (**Fig. 6I-J',N).** Lastly, we tested whether the loss of K16 has an impact on the aggregation and subsequent activation of MAVS (Hou et al., 2011) in the IMQ model *in vivo.* Staining for MAVS in skin tissue sections revealed an increased number of aggregates in the epidermis of IMQ-treated WT mice relative to control **(Fig. 6K-L',O)**. The frequency of MAVS aggregates was significantly increased in *Krt16* null mouse epidermis, further supporting a mechanism whereby loss of K16 leads to increased interactions between 14-3-3 and RIG-I and hyperactivation of MAVS and IFN response genes.

Discussion

The findings reported here identify a role for K16 as a stress-responsive, spatially restricted inhibitor of type-I interferon signaling in the suprabasal interfollicular epidermis. In the mouse model of imiquimod-induced psoriasiform disease, loss of K16 leads to exacerbation of phenotypes and amplified IFN signaling in the suprabasal, differentiating compartment of the epidermis, where stress-induced K16 is normally expressed. Similarly, loss of IFN restriction and amplified inflammation were observed in *Krt16* null mice subjected to an acute model of sterile inflammation. Our studies in differentiated N/TERT human keratinocytes *ex vivo* recapitulate the findings from mouse models and provide molecular mechanistic insight underlying the amplified inflammatory response. *Ex vivo,* we identified that K16 interacts with 14-3-3ε, a regulator of RLR signaling upstream of IFN activation. *In vivo,* we identified that imiquimod-treated *Krt16* null mice

show increased proximity between 14-3-3ε and RIG-I signaling, and consequent aggregation of downstream MAVS protein, upstream of IRF-7 phosphorylation and IFN activation. These findings highlight a crucial role for K16 in stress and immune responses through regulation of Type I interferon signaling.

Identifying a role for K16 in regulating interferon signaling ties directly to its use as a biomarker in inflammatory skin diseases with aberrant interferon signaling, e.g., psoriasis ,hidradenitis suppurativa and atopic dermatitis (Jiang et al., 2015; Nguyen et al., 2021; Renert-Yuval et al., 2021). Studies have implicated Type I interferon signaling in the initiation of psoriatic lesions through the Koebner phenomenon (Zhang, 2019) and in keratinocyte responses during skin injury (Zhang et al., 2016). In the Koebner phenomenon, activation of keratinocytes by dsRNA or the antimicrobial peptide LL-37 is thought to trigger the psoriatic autoimmune cascade via upregulation of Type I interferon signaling. The Koebner phenomenon contributes to the pathogenesis of several diseases including vitiligo, psoriasis and lichen planus (Zhang et al., 2023). In addition to autoimmune diseases, the crucial role of Type-I interferon signaling in antiviral response has made the pathway, and its regulation, of high interest towards understanding both antiviral response and resulting inflammation. The regulation of RIG-I/MDA5/MAVS signaling through 14-3-3ε was first identified in studies of hepatitis C virus (Liu et al., 2012). Since then, accumulating evidence has suggested that herpesviruses target 14-3-3ε binding to inhibit IFN signaling (Awasthi et al., 2024; Gupta et al., 2020; Gupta et al., 2019), a mechanism similar to that observed in our study of keratin 16. Investigating whether RLRs and IFN signaling are regulated by other keratins capable of binding 14-3-3 isoforms (see below) warrant further study as it could be relevant to additional diseases.

Our observations suggest that high expression of K16 in the context of inflammatory skin diseases reflects keratinocytes' attempts to return to a ‘de-activated’ state. This hypothesis aligns with findings that mutations in K16 are associated with moderate but not mild psoriasis (Elango et al., 2018), supporting K16’s role as an inhibitor of inflammatory responses in keratinocytes. Of interest, in the interfollicular epidermis, K16 induction is dynamic (stress-responsive) and spatially regulated (suprabasal). Our observations thus suggest that K16’s role in the regulation of immune recruitment is tied

to keratinocyte differentiation, and represent a novel pathway by which the compartments of the epidermis differentially respond to stress.

While we report that the RIG-I/MDA5/MAVS pathway is affected by the loss of K16, the plethora of contexts and molecular signaling pathways involved in defining K16's role remains to be further studied. We previously showed that challenging *Krt16* null mouse skin with injury or topical TPA hyperactivate alarmins (Lessard et al., 2013), specifically S100A15 (also known as S100A7A or Koebnerisin), which is highly expressed in keratinocytes of psoriatic lesions (Batycka-Baran et al., 2014). Whether K16 regulates similar molecular pathways during wound healing, the response to UV, or in additional inflammatory diseases remains to be explored. Of note, neither of the topical treatment paradigms studied here *in vivo* (IMQ, TPA) are direct activators of RIG-I/MDA5/MAVS pathway. However, both paradigms are associated with release of damage-associated molecular patterns (DAMPs) (Lessard et al., 2013; Ma et al., 2024), activation of IFN responsive genes (Swindell et al., 2017; Xu et al., 2024b), and regulation by 14-3-3 family of proteins (Pennington et al., 2018). Recent studies have also identified an increase in RIG-I levels in keratinocytes treated with IMQ (Zhu et al., 2017), and showcased LL-37, an activator of RIG-I, as involved in psoriasis (Kahlenberg and Kaplan, 2013). The K16 IP/MS data reported here identified several additional targets and pathways that interact with K16 and provides a resource to test for additional molecular mechanisms through which K16 might alter immune responses in the suprabasal epidermis of stressed skin.

Despite their high homology, overlapping distribution, and involvement in disease (Cohen et al., 2024), the stress-responsive K16 and K17 exert a profoundly distinct impact on inflammation and innate immunity. Recently, our group identified a role for K17 at the early stage of the amplified recruitment of immune responses when the interfollicular epidermis is subjected to repeated stress (Xu et al., 2024b). In this instance, K17 is required for the sustained activation of PKCα in stressed keratinocytes. That K16 and K17 would exert opposite influences on immune recruitment in the skin, acting via distinct mechanisms, represents a novel and unanticipated reality. In patients with inflammatory diseases, K16 and K17 are co-expressed in a large population of keratinocytes at the transcriptional level (Cohen et al., 2024). This said, keratinocytes exhibiting a *KRT16*^{high}-

KRT17^{low} vs. a KRT16^{low}-KRT17^{high} character exhibit distinct transcriptional profiles and are correlated to different immune pathways (Cohen et al., 2024). Our observation of K16 S44 phosphorylation after TPA treatment potentially adds a layer, namely post-translation specification, to what has been recently described as a “keratin code” (Di Russo et al., 2023). The molecular structure of keratins and their relationship to their type II pairing partner can also play a role in how K16 and K17 differentially relate to effectors of innate immunity. In both human and mouse, for instance, the stability of K6-K17 heterocomplexes is markedly higher than that of K6-K16 ones, a difference mediated by determinants located within a specific segment of the central α-helical domain (Bernot et al., 2005; Wawersik et al., 1997). Thus, the dynamic regulation of stress-responsive keratins at the transcriptional, translational and post-translational levels suggests complex, multi-layered regulatory mechanisms that tie to pathways controlling both inflammation and recovery. Such context-dependent regulation of keratins, at multiple levels, is poised to impact their association with cellular proteins with roles in cellular signaling. Our results identified several interactions involving K16 and RLR and IFN response proteins, including 14-3-3 and TRIM proteins. Interactions between 14-3-3 and keratin proteins have previously been shown to regulate various cellular signaling pathways, including YAP-related progenitor status (K14:14-3-3sigma; Guo et al., 2020), mTOR (K17:14-3-3sigma; Pan et al., 2011), mitotic progression (K18:14-3-3zeta; Ku et al., 2002) and cell adhesion (K19:14-3-3; Mariani et al., 2020). How keratin:14-3-3 binding partnerships might regulate such a broad variety of molecular pathways remain ill-understood, and represents a future direction likely to yield significant insights into our understanding of keratin roles and regulation of cellular signaling.

The emerging role of keratins in regulating immune responses in stressed skin could also be relevant to their role during development and differentiation of ectoderm-derived appendages and palmoplantar epidermis (Bernot et al., 2002; Zieman et al., 2019). This is a distinct possibility as mutations in *KRT16* and other stress-responsive keratins are causative for Pachyonychia Congenita (PC), while mice null for *Krt16* exhibit aberrant differentiation and oxidative stress during development and homeostasis of palmoplantar skin (Kerns et al., 2016; Lessard and Coulombe, 2012; Zieman et al., 2019). Recent research has identified roles for IFN response in both healthy and diseased skin (Hile et

al., 2020), and accumulating evidence suggest significant roles for both immunity and 14-3-3ε during skin development (Gopee et al., 2024; Tilwani et al., 2024). Relevant to our findings, interferon response, hyperactivation of IRF7, and activation of MAVS have all been linked to oxidative stress and defective Nrf2 responses (Buskiewicz et al., 2016; Han et al., 2020; Thimmulappa et al., 2016). Intriguingly, use of a small molecule agonist to restore Nrf2 function and the cellular redox balance in keratinocytes prevents the formation of PPK-like lesions in the footpad skin of *Krt16* null mice (Kerns et al., 2016). Moreover, recent studies have identified a functional association between dsRNA, RIG-I protein and the expression of K9 (Zhou et al., 2019) a keratin specific to differentiated palmoplantar epidermis that is downregulated upon loss of K16 (Zieman et al., 2019). The prospect of complex interactions between RLR activation, IFN signaling, oxidative stress and keratin expression remains to be characterized and could be highly significant for our understanding of palmoplantar development and formation of PPK lesions in PC patients.

Altogether, the findings reported here identify a novel role for K16 in regulating Type I IFN signaling in the context of inflammatory diseases of the skin. Our results provide insight into how keratin expression, and its spatial restriction, can inform epithelial-immune crosstalk. Such insight is highly important for a better understanding of chronic inflammatory skin diseases.

Methods

Study approval and ethics statement

This study utilized histological sections of lesional and non-lesional skin from humans and was approved by the University of Michigan Institutional Review Board (HUM00174864). Participants gave informed consent to participate in a study conducted according to the Declaration of Helsinki Principles. Heparinized whole blood from anonymous healthy human donors was obtained by venipuncture from the Platelet Pharmacology and Physiology Core at the University of Michigan (IRB#HUM00107120). All samples were deidentified and study authors did not have access to the relevant HIPAA information.

Single cell RNAseq analyses

Single cell RNAseq datasets from human psoriatic lesional skin and HS were originally published by (Cheng et al., 2018; Gudjonsson et al., 2020; Ma et al., 2023) and made publicly available at EGAS00001002927 (PSOR), GSE173706 (PSOR) and GSE154775 (HS) GSE154773 (HS). The datasets were reanalyzed using Seurat's SCTransform "v2" as detailed in (Cohen et al., 2024). Within each dataset, differentially-expressed genes in high vs. low *KRT16*-expressing keratinocytes were identified by comparing top quartiles ("*KRT16*^{high}") vs. lowest quartiles ("*KRT16*^{low}") cells. Differentially expressed genes (adjP<0.05) were then plotted for fold-change and "difference % expression between populations". Spatial transcriptomics was performed by embedding tissues into a single block, followed by a 5 µm section mounted onto CosMX slide (Nanostring). CosMx spatial library generation and transcriptomics was completed using the manufacturer's instructions, with tissue sections hybridized with fluorescently labeled oligonucleotide probes targeting specific mRNAs, using the standard custom 1,000 panel.

Analysis of Microarray data from PC patients and *Krt16*$^{-/-}$ mouse lesional skin

Microarray datasets were previously published and analyzed (Cao et al., 2015; Zieman et al., 2019). For the human PC study (Cao et al., 2015), gene expression data for patients with K16 and K6 mutations was downloaded, filtered, and analyzed for average p-value across patients. Differentially-expressed genes were analyzed using the Panther (Mi et al., 2013) and Reactome (Croft et al., 2010) freeware to identify pathways of significance. For *Krt16*$^{-/-}$ mouse microarray dataset, Affymetrix microarray .CEL files from GSE117375 were imported into R using the 'oligo' package of Bioconductor.org. Raw Affymetrix probe data were summarized to ENTREZ IDs using version 23 custom Chip Definition Files (CDFs) (Dai et al., 2005). Data were quantile-normalized using the Robus Multi-Array Average (RMA) technique. The limma package of Bioconductor.org was used to fit array quality weights (Ritchie et al., 2006) and linear models with the empirical bayes method to test differences between *Krt16* null and WT samples (Smyth, 2004). Significant genes were defined by a Benjamini–Hochberg FDR adjusted P-value of .05 or less and a log2 fold change of 1.5 or greater. Conditional hypergeometric tests were used in the GOstats package or Bioconductor.org, conditioned so that parent terms were not tested with genes of a significant child term.

Immunoprecipitation and Mass Spectrometry of cultured keratinocyte proteins

Analysis of the Flag-K16 interactome in cultured HaCat keratinocytes (Boukamp et al., 1988) was done in triplicate as follows. HaCat cells were transfected with K16-flag construct or empty vector (EV) control using the nucleofector cell line SE kit, with 500K cells per well and 0.6ug of DNA. Cells were seeded a 6-well plate and allowed to recover for 24h. Cells were then lysed using NETN lysis buffer (150mM NaCl, 1mM EDTA – ethylenediaminetetraacetic acid, 20mM tris buffer pH 8.0 and 0.5% v/v Nonidet P-40) supplemented with Pierce™ Phospho-stop phosphatase inhibitor tablets (Thermofisher Scientific) and cOmplete™protease EDTA-free inhibitor (Millipore Sigma). Samples were bound to the anti-flag M2 magnetic beads (Sigma-Aldrich) and blotted for TCHP, K16 and FLAG to control for pulldown efficiency. Elutes were then submitted to the University of Michigan Proteomics Resource Facility for LC-MS/MS analysis. Data was analyzed with proteome discoverer 2.4 and The Contaminant Repository for Affinity Purification (Mellacheruvu et al., 2013) to derive significant interactions (adjP<0.05) and Significance Analysis of INTeractome (SAINT) scores (Choi et al., 2011). Results were analyzed by String-DB (Szklarczyk et al., 2023) to generate an interactome network between the most highly significant genes (SAINT <0.8). Last, the list of the top 326 significant interacting proteins was subjected to statistical overrepresentation analysis using Panther (Mi et al., 2013) and Reactome (Croft et al., 2010) freeware. Significant pathways (FDR adjP<0.05) were retained for consideration.

For immunoprecipitation of endogenous K16 protein from post-confluent, bilayered N/TERT keratinocyte cultures, untreated, Poly(I:C) treated (6h), or Poly(I:C) treated and recovered (6h + 24h recovery) WT and *KRT16* KO cells were lysed using NETN lysis buffer. Samples were assessed for protein concentration using the Pierce BCA assay and 35ug proteins was used as input for the immunoprecipitation. Samples were bound to Dyanbeads protein G (Fisher Scientific) with 2μg anti-K16 antibody (Santa Cruz Biotechnology, #sc-53255), and immunoprecipitated following manufacturer instructions. Elutes were blotted for K16 to control for pulldown efficiency, 14-3-3ε, and cofilin as the input loading control. Last, single replicates of K16 immunoprecipitated elutes (50μg) from untreated and poly(I:C) treated and recovered samples were submitted for University of Michigan Proteomics Resource Facility for LC-MS/MS. Data was analyzed with proteome

discoverer 2.4 against SwissProt human protein database and provided as additional supplement (see Supplemental Table 1).

Mass spectrometry-based analysis of mouse ear skin proteins

Dorsal ear skin samples were collected at 0, 6, 12, 24 and 48h after TPA treatment (4ug, topical). Samples were then resuspended in 8M Urea buffer (50mM Tris-HCl pH 8.5, 8M urea, 1mM EGTA, 1mM PMSF, 2mM DTT) supplemented with Pierce™ Phospho-stop phosphatase inhibitor tablets (Thermofisher Scientific) and cOmplete™ EDTA-free protease inhibitor (Millipore Sigma). After homogenization, lysates were centrifuged at 16,000 × g for 10 min at 4°C and cleared supernatants collected. Samples were boiled with 4× Laemmli sample buffer containing 10% β-mercaptoethanol (BME) at 95°C for 10 minutes and loaded onto an SDS-PAGE gel. Gel pieces from the 50kDa migration area were dissected from the Coomassie-stained gel and digested with Trypsin/Lys-C mix (#PAV5073, Promega) after reduction with 10mM Dithiothreitol and alkylation with 50 mM 2-Chloroacetamine (#C0267, Sigma-Aldrich). The resulting peptides were labeled with TMT10plex Isobaric Label reagents (#90110, ThermoFisher Scientific) according to the manufacturer's instructions (Labels used:126-0hr; 127N-0hr; 128N-TPA 6h; 129N-TPA 6h; 130N-TPA 12h; 131-TPA 12h; 127C-TPA 24h; 128C-TPA 24h; 129C-TPA 48h; 130C-TPA 48h). Pooled samples were desalted with Sep-Pak solid phase extraction columns. For the phosphorylation analysis, High-Select TiO2 phosphopeptide enrichment kit (A32993, ThermoFisher Scientific) was used according to manufacturer protocol. Protein samples were then processed at the Mass Spectrometry Facility of the Department of Pathology at the University of Michigan, and analyzed using an Orbitrap Ascend Tribrid mass spectrometer (Thermo Fisher Scientific) equipped with an FAIMS source with Vanquish Neo UHPLC. Specifically, MS Samples were analyzed in a 120 min gradient using three compensation voltages (CVs) -40, -55 and -70 V. The full scans (MS1) were acquired over a mass-to-charge (m/z) range of 400-1600 m/z (Orbitrap); the resolution was set to 120K and AGC target 400000; the maximum injection time is 251 ms. Precursor ions with charge states of 2-6 were isolated at 0.7 m/z width and fragmented by HCD (NCE 38%; normalized AGC target of 200%; 45Kresolution; max injection time 50 ms). Dynamic exclusion was 60 seconds. Proteome Discoverer (Thermo Fisher) was used for data analysis and spectra were searched against the Mus musculus UniProt FASTA

database (UP000000589). MS1 and MS2 tolerance were set to 10 ppm and 0.6 Da, respectively, and enzyme specificity was set to trypsin with up to two missed cleavages. The search included carbamido-methylation of cysteines and TMT labeling of lysine and N-termini of peptides as fixed modifications; and oxidation of methionine, deamidation of asparagine, glutamine and phosphorylation of serine, threonine, tyrosine as variable modification. Identified proteins and peptides were filtered according to ≤1% FDR threshold.

Mouse models and treatment

All experiments were performed on 8-12 weeks old male mice in FVB background and were approved by the Institutional Animal Use and Care Committee at the University of Michigan Medical School. *Krt16*$^{-/-}$ mouse were previously described and characterized (Lessard and Coulombe, 2012). For imiquimod application, *Krt16*$^{-/-}$ or WT littermate mice were anesthetized with isoflurane 2 days prior to the experiment (day -2) and had a 60x25mm area of their back skin shaved. Mice were then housed individually for the duration of the experiment. After two days ("day 0"), Imiquimod (5% Aldara™ cream) or Vaseline was applied to the shaved area using a sterile pipette tip under anesthesia. Mice were returned to their housing and treated daily using the same protocol for 4 additional days. At day 5, mice were euthanized and back skin tissue collected for sectioning and analysis. Cryosectioning was performed using CRYOSTAR NX50 Cryostat (Thermo Scientific) and MX35 ultramicrotome blade (Epredia #3053835). Tissues were cut at 5-µm cross-sections and placed on charged microscope slides (VWR #48311–703). Sections were either stained immediately after or stored at −40°C until further use. Application of single or double dose of TPA (Cell Signaling Technology #4174S), or Acetone vehicle control, to dorsal ear has been previously described in detail (Xu et al., 2024b). Briefly, *Krt16*$^{-/-}$ or WT littermate mice were treated with single (at 0 h) or double (at 0h and 24h) applications of 20 µl of 0.2 mg/ml of TPA (Cell Signaling Technology), on the dorsal side of ear skin, with the other ear treated with acetone vehicle control. Ear samples were collected at 6h after final application and kept at -40°C for cryosectioning.

Indirect immunofluorescence analysis of mouse and human skin sections

Both mouse and human skin sections were stained using a previously described protocol (Xu et al 2024b). In summary, sections were fixed using 4% paraformaldehyde (PFA, Electron Microscopy Science*)* for 10 min, washed three times with 1X PBS for 5 minutes, and a circle was drawn around tissue pieces with hydrophobic barrier pen (CALIBIOCHEM #402176). Sections were then blocked with blocking buffer (2% normal goat or donkey serum, 1% bovine serum albumin in 1× PBS) for 30-60 minutes at room temperature. Antibodies diluted in blocking buffer (see appended list of antibodies*)* were applied in a humid chamber for 2 hours at 37°C. Sections were washed three times with PBS and stained with secondary Alexa-fluor conjugated antibodies (Invitrogen) and DAPI. Last, coverslips (VWR, 1.5 thickness) were mounted using VECTASHIELD® Anti-fade Mounting Medium (Vector Laboratories) for confocal imaging. All sections were imaged for full z-dimensions using a Zeiss LSM800 confocal microscope and analyzed in ImageJ or CellProfiler as detailed in the 'Image quantification and statistical analyses' section. Histological analysis using hematoxylin (Thermo Scientific, TA-060-MH) & eosin (Thermo Scientific, 71204) staining was performed per Sigma-Aldrich Procedure No. MHS #1 and images were acquired using a Zeiss fluorescence microscope.

Post-confluent cultures of human N/TERT keratinocytes and CRISPR/Cas9 editing

N/TERT keratinocytes were grown in Keratinocyte SFM media, supplemented with epidermal growth factor (rEGF, 0.2ng/ml), bovine pituitary extract (BPE, 30 ug/ml), calcium chloride (0.31mM) and penicillin streptomycin (10 units/ml). N/TERT cells were seeded at 300,000 (100mm plate) or at 30,000 cells (6 well plate), with media replaced every 48 h. Cells were monitored daily for confluence and monitored for formation of bilayer. At 4 d post confluence, cells were subjected to treatment (Poly(I:C) or TPA) and processed for imaging, lysis or collection of conditioned media. Generation of CRISPR knock-out (KO) cell lines using non-homologous end joining (NHEJ) via CRISPR/Cas9 and baricitinib was completed by the Functional Analytics CRISPR Core of the University of Michigan Skin Research Center as described (Sarkar et al., 2023). Specifically, sgRNA was designed for *KRT16* unique region (5' GCCTGTCTGTCTCCTCTCGCTTC 3'). In total, 38 clones were generated and tested for *KRT16* DNA and RNA (cDNA Synthesis Kit, Thermofisher Scientific), and proteins levels were assessed by immuno-

blotting and staining with K16 antibody. A single clone (#32) showed complete K16 protein KO, secondary to a 4bp deletion and frameshift at amino acid 49, leading to an early stop codon at position 117. To control for non-specific CRISPR phenotypes, CRISPR KO for the tubulin alpha pseudogene was generated (5' GTATTCCGTGGGTGAACGGG 3'), referred to as 'MOCK' controls, as previously described (Xu et al., 2024a).

TPA and PolyIC treatment of N/TERT keratinocyte cultures

For treatment of N/TERT keratinocytes with Polyinosinic- polycytidylic acid sodium salt (poly(I:C), Millipore Sigma), N/TERT keratinocytes were grown to 4 d post-confluence and subjected to: (1) no treatment, (2) 6h treatment with poly(I:C) at 10ug/ml or (3) 6h Poly(I:C) followed by 24h recovery in KSFM media. Cells were fixed with 4% PFA for indirect immunofluorescence or lysed with 6.5M urea buffer (50 mM Tris-HCl pH 7.5, 150 mM NaCL, 5 mM EDTA, 1% Triton X-100, 6.5 M Urea) supplemented with Pierce™ Phospho-stop phosphatase inhibitor tablets (Thermofisher Scientific) and cOmplete™protease EDTA-free inhibitor (Millipore Sigma) for immunoblotting. Both methods were previously described in detail (Xu et al., 2024b). Conditioned media was collected from untreated or poly(I:C) treated+24h recovered cells using a 3 ml syringe (BD Syringe) with a 0.22 µm PVDF syringe filter (Millipore #SLGVM33RS) and stored at −20°C until use in neutrophil transwell migration assay as previously described (Xu et al., 2024b). For TPA treatment, cells were subjected to (1) 200nM TPA in KSFM media or (2) acetone vehicle control in KSFM media for 6h, followed by a 24h recovery in untreated KSFM media. Conditioned media was then collected from the cells and subjected to neutrophil transwell migration assay.

Proximity ligation assays

Proximity ligation assays (PLA) were conducted using Duolink PLA Fluorescence kit (Millipore Sigma). To reduce background noise, additional washes were implemented in addition to the manufacturer instructions. In brief, cultured cells or tissue sections were fixed in 4% PFA solution for 20 minutes, and permeabilized with 0.1% Triton X-100 for 10 min at room temperature. Samples were washed 3x with PBS and blocked with either 5% normal goat serum (N/TERT keratinocytes) or 2% normal goat serum, 1% bovine serum

albumin (tissue sections) for 16h at 4°C. Primary antibodies were then diluted in blocking buffer and added to sample in a humid chamber for 1h at 37°C. Cells were then washed (1xPBS, 3 times, 5 min) and incubated with PLA probes, ligation mixture and amplification mixture according to the manufacturer's instructions. Washes with buffers (A, B , 0.01x B) were doubled from manufacturer recommended time and length to improve the signal to noise ratio.

Image quantification and statistical analyses

Quantitation of immunofluorescence, PLA, and western blots were performed using ImageJ (Schneider et al., 2012) and CellProfiler 4.2.7 (Stirling et al., 2021). Quantification of PLA dots was performed as follows: max z-projection was applied to the images, and primary objects were identified using Otsu two-class threshold for Nuclei (smoothing scale 3; threshold correlation factor 0.5), and Manual threshold strategy for PLA dots (0.05 threshold with 1.344 default smoothing scale). Cells were identified as secondary object based on distance between nuclei (up to 10 µm from the nuclear periphery) using an adaptive Otsu three-class threshold strategy (smoothing scale 10, correlation factor 1). Cells touching the border of the image were discarded from analysis. Outlines of all objects (nuclei, PLA, cells) were saved to provide manual validation and documentation of the analysis. Last, the number of PLA dots per cells was exported and reported. For quantification of immunofluorescence in keratinocytes, sum z-projections were generated for each N/TERT layer and subjected to CellProfiler analysis as described above. Fluorescence intensity for immunostaining (ISG15, pIRF7, RIG-I), and object diameter (nuclei) were calculated per object and results were exported to spreadsheet. Last, to quantify MAVS aggregates, a 165x45um ROI from the suprabasal layer was generated in ImageJ, transformed with max z-projection and used as input for CellProfiler. MAVS aggregates were then identified using a set diameter (5-10 units) and manual thresholding (0.15 threshold with 1.344 default smoothing scale).

For *in vivo* mitotic index analysis, individual cells were counted using ImageJ and categorized based on their Ki67 staining and location with respect to basal or suprabasal layer of epidermis. Mitotic index (Ki67+/total cells) was reported for WT and *Krt16*$^{-/-}$ littermates, and analysis of suprabasal mitoses was done in IMQ-treated mice. No

suprabasal mitoses were observed in vaseline controls. *In vivo* OAS1 levels were calculated by generating ROI around the epidermis and calculating mean intensity. Additionally, line profiles (width 200pixels) were generated from dermal-epidermal interface to the stratum corneum, and OAS1 signal per distance were recorded. Results across technical replicates (at least 3 lines per section and 3 sections per animal), and animals (at least 3 animals per condition) were aggregated and provided as mean +/- SE in a graphs of OAS1 levels per distance from basement membrane. *In vivo* neutrophil infiltration levels were calculated as the area fraction of Ly6g-positive staining in the TPA-treated skin subtracted by background as previously analyzed (Xu et al., 2024b).

Error bars on histograms represent standard error of the mean (SEM) across biological replicates. All experimental conditions were done with at least 3 biological replicates performed as different batches (separate littermates, separate culture), with at least 2 technical replicates used per biological sample (tissue sections, confocal images, SDS page). Statistical significance was determined by one-way ANOVA followed by Tukey's multiple comparisons test, Sidak's multiple comparisons test, and paired or unpaired *t* test. Test information is detailed in the appropriate figure legends. Differences with $p < 0.05$ were considered statistically significant and p values are noted as ns (p>0.05), * (p<0.05), ** (p<0.01), *** (p<0.001) and **** (p< *0.0001).* Graphs generation and all statistical analyses were performed using GraphPad Prism v10.2.2.

List of antibodies used in study

A list of antibodies and their use is provided in Supplementary Table 2.

Acknowledgments

The authors are grateful to members of the Coulombe and Parent laboratories for advice, to Dr. Venkatesha Basrur and the Proteomics Resource Facility in Department of Pathology at the Univ. of Michigan for mass spectrometry analyses, to the Platelet Pharmacology and Physiology Core at the Univ. of Michigan for providing primary human neutrophils, and to the Skin Biology Center for providing NTERT keratinocytes. EC received fellowship support from the National Institutes of Health (NIH; grant T32

AR007197) and from the National Psoriasis Foundation. JG and MKS were supported by NIH grant P30 AR075043. These studies were supported by grant R01 AR083822 (to PAC and CAP) from the NIH.

Contributions

EC and PAC together designed the study and analyzed all findings. CAP contributed to the design and interpretation of all experiments involving neutrophils. EC led the studies involving mice and cultured cells with assistance from YX, AO, and DW. KS led the effort to produce a K16 interactome in HaCaT keratinocytes, and NO led analyses involving mass spectrometry. CJ and EC analyzed the single-cell RNAseq datasets, and EC led the effort of integrating them in a shared conceptual framework. MS and JE provided the parental and *KRT16* null N/TERT cell lines, and JE provided key expertise in interferon signaling and chronic inflammatory skin diseases. EC wrote the initial version of the manuscript with input from PAC.

References

Awasthi, P., D. Kumar, and S. Hasan. 2024. Role of 14-3-3 protein family in the pathobiology of EBV in immortalized B cells and Alzheimer's disease. *Frontiers in Molecular Biosciences* 11:1353828.

Batycka-Baran, A., J. Maj, R. Wolf, and J. Szepietowski. 2014. The new insight into the role of antimicrobial proteins-alarmins in the immunopathogenesis of psoriasis. *Journal of immunology research* 2014:628289.

Bernot, K.M., P.A. Coulombe, and K.M. McGowan. 2002. Keratin 16 expression defines a subset of epithelial cells during skin morphogenesis and the hair cycle. *Journal of investigative dermatology* 119:1137-1149.

Bernot, K.M., C.-H. Lee, and P.A. Coulombe. 2005. A small surface hydrophobic stripe in the coiled-coil domain of type I keratins mediates tetramer stability. *The Journal of cell biology* 168:965-974.

Boelsma, E., M.C. Verhoeven, and M. Ponec. 1999. Reconstruction of a human skin equivalent using a spontaneously transformed keratinocyte cell line (HaCaT). *Journal of investigative dermatology* 112:489-498.

Boukamp, P., R.T. Petrussevska, D. Breitkreutz, J. Hornung, A. Markham, and N.E. Fusenig. 1988. Normal keratinization in a spontaneously immortalized aneuploid human keratinocyte cell line. *The Journal of cell biology* 106:761-771.

Buskiewicz, I.A., T. Montgomery, E.C. Yasewicz, S.A. Huber, M.P. Murphy, R.C. Hartley, R. Kelly, M.K. Crow, A. Perl, and R.C. Budd. 2016. Reactive oxygen species induce virus-independent MAVS oligomerization in systemic lupus erythematosus. *Science signaling* 9:ra115-ra115.

Cao, Y.-A., R.P. Hickerson, B.L. Seegmiller, D. Grapov, M.M. Gross, M.R. Bessette, B.S. Phinney, M.A. Flores, T.J. Speaker, and A. Vermeulen. 2015. Gene expression profiling in pachyonychia congenita skin. *Journal of dermatological science* 77:156-165.

Cheng, J.B., A.J. Sedgewick, A.I. Finnegan, P. Harirchian, J. Lee, S. Kwon, M.S. Fassett, J. Golovato, M. Gray, and R. Ghadially. 2018. Transcriptional programming of normal and inflamed human epidermis at single-cell resolution. *Cell reports* 25:871-883.

Choi, H., B. Larsen, Z.-Y. Lin, A. Breitkreutz, D. Mellacheruvu, D. Fermin, Z.S. Qin, M. Tyers, A.-C. Gingras, and A.I. Nesvizhskii. 2011. SAINT: probabilistic scoring of affinity purification–mass spectrometry data. *Nature methods* 8:70-73.

Christian, F., E.L. Smith, and R.J. Carmody. 2016. The regulation of NF-κB subunits by phosphorylation. *Cells* 5:12.

Cohen, E., C. Johnson, C.J. Redmond, R.R. Nair, and P.A. Coulombe. 2022. Revisiting the significance of keratin expression in complex epithelia. *Journal of Cell Science* 135:jcs260594.

Cohen, E., C.N. Johnson, R. Wasikowski, A.C. Billi, L.C. Tsoi, J.M. Kahlenberg, J.E. Gudjonsson, and P.A. Coulombe. 2024. Significance of stress keratin expression in normal and diseased epithelia. *Iscience* 27:

Croft, D., G. O'kelly, G. Wu, R. Haw, M. Gillespie, L. Matthews, M. Caudy, P. Garapati, G. Gopinath, and B. Jassal. 2010. Reactome: a database of reactions, pathways and biological processes. *Nucleic acids research* 39:D691-D697.

Dai, M., P. Wang, A.D. Boyd, G. Kostov, B. Athey, E.G. Jones, W.E. Bunney, R.M. Myers, T.P. Speed, and H. Akil. 2005. Evolving gene/transcript definitions significantly alter the interpretation of GeneChip data. *Nucleic acids research* 33:e175-e175.

Der, S.D., A. Zhou, B.R. Williams, and R.H. Silverman. 1998. Identification of genes differentially regulated by interferon α, β, or γ using oligonucleotide arrays. *Proceedings of the National Academy of Sciences* 95:15623-15628.

Di Russo, J., T.M. Magin, and R.E. Leube. 2023. A keratin code defines the textile nature of epithelial tissue architecture. *Current Opinion in Cell Biology* 85:102236.
Dickson, M.A., W.C. Hahn, Y. Ino, V. Ronfard, J.Y. Wu, R.A. Weinberg, D.N. Louis, F.P. Li, and J.G. Rheinwald. 2000. Human keratinocytes that express hTERT and also bypass a p16INK4a-enforced mechanism that limits life span become immortal yet retain normal growth and differentiation characteristics. *Molecular and cellular biology* 20:1436-1447.
Dickson, M.C., V.J. Ludbrook, H.C. Perry, P.A. Wilson, S.J. Garthside, and M.H. Binks. 2015. A model of skin inflammation in humans leads to a rapid and reproducible increase in the interferon response signature: a potential translational model for drug development. *Inflammation Research* 64:171-183.
Elango, T., J. Sun, C. Zhu, F. Zhou, Y. Zhang, L. Sun, S. Yang, and X. Zhang. 2018. Mutational analysis of epidermal and hyperproliferative type I keratins in mild and moderate psoriasis vulgaris patients: a possible role in the pathogenesis of psoriasis along with disease severity. *Human genomics* 12:1-21.
Feng, X., H. Zhang, J.B. Margolick, and P.A. Coulombe. 2012. Keratin intracellular concentration revisited: implications for keratin function in surface epithelia. *The Journal of investigative dermatology* 133:850.
Fuchs, E., and D.W. Cleveland. 1998. A structural scaffolding of intermediate filaments in health and disease. *Science* 279:514-519.
Gallegos-Alcalá, P., M. Jiménez, D. Cervantes-García, and E. Salinas. 2021. The keratinocyte as a crucial cell in the predisposition, onset, progression, therapy and study of the atopic dermatitis. *International Journal of Molecular Sciences* 22:10661.
Gopee, N.H., E. Winheim, B. Olabi, C. Admane, A.R. Foster, N. Huang, R.A. Botting, F. Torabi, D. Sumanaweera, and A.P. Le. 2024. A prenatal skin atlas reveals immune regulation of human skin morphogenesis. *Nature* 1-11.
Gudjonsson, J.E., L.C. Tsoi, F. Ma, A.C. Billi, K.R. van Straalen, A.R. Vossen, H. van der Zee, P.W. Harms, R. Wasikowski, and C.M. Yee. 2020. Contribution of plasma cells and B cells to hidradenitis suppurativa pathogenesis. *JCI insight* 5:
Guo, Y., C.J. Redmond, K.A. Leacock, M.V. Brovkina, S. Ji, V. Jaskula-Ranga, and P.A. Coulombe. 2020. Keratin 14-dependent disulfides regulate epidermal homeostasis and barrier function via 14-3-3σ and YAP1. *Elife* 9:e53165.
Gupta, S., P. Ylä-Anttila, T. Sandalova, A. Achour, and M.G. Masucci. 2020. Interaction with 14-3-3 correlates with inactivation of the RIG-I signalosome by herpesvirus ubiquitin deconjugases. *Frontiers in Immunology* 11:437.
Gupta, S., P. Ylä-Anttila, T. Sandalova, R. Sun, A. Achour, and M.G. Masucci. 2019. 14-3-3 scaffold proteins mediate the inactivation of trim25 and inhibition of the type I interferon response by herpesvirus deconjugases. *PLoS pathogens* 15:e1008146.
Han, S., H. Zhuang, P.Y. Lee, M. Li, L. Yang, P.A. Nigrovic, and W.H. Reeves. 2020. NF-E2–related factor 2 regulates interferon receptor expression and alters macrophage polarization in lupus. *Arthritis & Rheumatology* 72:1707-1720.
Hile, G.A., J.E. Gudjonsson, and J.M. Kahlenberg. 2020. The influence of interferon on healthy and diseased skin. *Cytokine* 132:154605.
Hobbs, R.P., J.C. Lessard, and P.A. Coulombe. 2012. Keratin intermediate filament proteins–novel regulators of inflammation and immunity in skin. *Journal of cell science* 125:5257-5258.
Hou, F., L. Sun, H. Zheng, B. Skaug, Q.-X. Jiang, and Z.J. Chen. 2011. MAVS forms functional prion-like aggregates to activate and propagate antiviral innate immune response. *Cell* 146:448-461.
Huang, Y.-Z., Y.-X. Zheng, Y. Zhou, F. Xu, Y.-Z. Cui, X.-Y. Chen, Z.-Y. Wang, B.-X. Yan, M. Zheng, and X.-Y. Man. 2022. OAS1, OAS2, and OAS3 contribute to epidermal keratinocyte proliferation by regulating cell cycle and augmenting IFN-1–Induced jak1–

signal transducer and activator of transcription 1 phosphorylation in psoriasis. *Journal of Investigative Dermatology* 142:2635-2645. e2639.
Jiang, S., T.E. Hinchliffe, and T. Wu. 2015. Biomarkers of an autoimmune skin disease—psoriasis. *Genomics, Proteomics and Bioinformatics* 13:224-233.
Kahlenberg, J.M., and M.J. Kaplan. 2013. Little peptide, big effects: the role of LL-37 in inflammation and autoimmune disease. *The Journal of Immunology* 191:4895-4901.
Kawai, T., and S. Akira. 2007. Signaling to NF-κB by Toll-like receptors. *Trends in molecular medicine* 13:460-469.
Kerns, M.L., J.M. Hakim, R.G. Lu, Y. Guo, A. Berroth, R.L. Kaspar, and P.A. Coulombe. 2016. Oxidative stress and dysfunctional NRF2 underlie pachyonychia congenita phenotypes. *The Journal of clinical investigation* 126:2356-2366.
Kim, S., P. Wong, and P.A. Coulombe. 2006. A keratin cytoskeletal protein regulates protein synthesis and epithelial cell growth. *Nature* 441:362-365.
Ku, N.-O., S. Michie, E.Z. Resurreccion, R.L. Broome, and M.B. Omary. 2002. Keratin binding to 14-3-3 proteins modulates keratin filaments and hepatocyte mitotic progression. *Proceedings of the National Academy of Sciences* 99:4373-4378.
Leachman, S.A., R.L. Kaspar, P. Fleckman, S.R. Florell, F.J. Smith, W.I. McLean, D.P. Lunny, L.M. Milstone, M.A. Van Steensel, and C.S. Munro. 2005. Clinical and pathological features of pachyonychia congenita. In Journal of Investigative Dermatology Symposium Proceedings. Elsevier, 3-17.
Lessard, J.C., and P.A. Coulombe. 2012. Keratin 16–null mice develop palmoplantar keratoderma, a hallmark feature of pachyonychia congenita and related disorders. *Journal of investigative dermatology* 132:1384-1391.
Lessard, J.C., S. Piña-Paz, J.D. Rotty, R.P. Hickerson, R.L. Kaspar, A. Balmain, and P.A. Coulombe. 2013. Keratin 16 regulates innate immunity in response to epidermal barrier breach. *Proceedings of the National Academy of Sciences* 110:19537-19542.
Li, P., K. Rietscher, H. Jopp, T.M. Magin, and M.B. Omary. 2023. Posttranslational modifications of keratins and their associated proteins as therapeutic targets in keratin diseases. *Current Opinion in Cell Biology* 85:102264.
Liao, J., and M.B. Omary. 1996. 14-3-3 proteins associate with phosphorylated simple epithelial keratins during cell cycle progression and act as a solubility cofactor. *The Journal of cell biology* 133:345-357.
Lin, R., C. Heylbroeck, P.M. Pitha, and J. Hiscott. 1998. Virus-dependent phosphorylation of the IRF-3 transcription factor regulates nuclear translocation, transactivation potential, and proteasome-mediated degradation. *Molecular and cellular biology*
Liu, H.M., Y.-M. Loo, S.M. Horner, G.A. Zornetzer, M.G. Katze, and M. Gale. 2012. The mitochondrial targeting chaperone 14-3-3ε regulates a RIG-I translocon that mediates membrane association and innate antiviral immunity. *Cell host & microbe* 11:528-537.
Ma, F., O. Plazyo, A.C. Billi, L.C. Tsoi, X. Xing, R. Wasikowski, M. Gharaee-Kermani, G. Hile, Y. Jiang, and P.W. Harms. 2023. Single cell and spatial sequencing define processes by which keratinocytes and fibroblasts amplify inflammatory responses in psoriasis. *Nature communications* 14:3455.
Ma, M., W. Jiang, and R. Zhou. 2024. DAMPs and DAMP-sensing receptors in inflammation and diseases. *Immunity* 57:752-771.
Madeira, F., M. Tinti, G. Murugesan, E. Berrett, M. Stafford, R. Toth, C. Cole, C. MacKintosh, and G.J. Barton. 2015. 14-3-3-Pred: improved methods to predict 14-3-3-binding phosphopeptides. *Bioinformatics* 31:2276-2283.
Mariani, R.A., S. Paranjpe, R. Dobrowolski, and G.F. Weber. 2020. 14-3-3 targets keratin intermediate filaments to mechanically sensitive cell–cell contacts. *Molecular biology of the cell* 31:930-943.

McLean, W., E. Rugg, D. Lunny, S. Morley, E. Lane, O. Swensson, P. Dopping-Hepenstal, W. Griffiths, R. Eady, and C. Higgins. 1995. Keratin 16 and keratin 17 mutations cause pachyonychia congenita. *Nature genetics* 9:273-278.

Mellacheruvu, D., Z. Wright, A.L. Couzens, J.-P. Lambert, N.A. St-Denis, T. Li, Y.V. Miteva, S. Hauri, M.E. Sardiu, and T.Y. Low. 2013. The CRAPome: a contaminant repository for affinity purification–mass spectrometry data. *Nature methods* 10:730-736.

Mi, H., A. Muruganujan, J.T. Casagrande, and P.D. Thomas. 2013. Large-scale gene function analysis with the PANTHER classification system. *Nature protocols* 8:1551-1566.

Moll, R., M. Divo, and L. Langbein. 2008. The human keratins: biology and pathology. *Histochemistry and cell biology* 129:705-733.

Morrison, D.K. 2009. The 14-3-3 proteins: integrators of diverse signaling cues that impact cell fate and cancer development. *Trends in cell biology* 19:16-23.

Nair, R.R., J. Hsu, J.T. Jacob, C.M. Pineda, R.P. Hobbs, and P.A. Coulombe. 2021. A role for keratin 17 during DNA damage response and tumor initiation. *Proceedings of the National Academy of Sciences* 118:e2020150118.

Nguyen, T.V., G. Damiani, L.A. Orenstein, I. Hamzavi, and G. Jemec. 2021. Hidradenitis suppurativa: an update on epidemiology, phenotypes, diagnosis, pathogenesis, comorbidities and quality of life. *Journal of the European Academy of Dermatology and Venereology* 35:50-61.

Ning, S., J. Pagano, and G. Barber. 2011. IRF7: activation, regulation, modification and function. *Genes & Immunity* 12:399-414.

Omary, M.B., P.A. Coulombe, and W.I. McLean. 2004. Intermediate filament proteins and their associated diseases. *New England Journal of Medicine* 351:2087-2100.

Pallari, H.-M., and J.E. Eriksson. 2006. Intermediate filaments as signaling platforms. *Science's STKE* 2006:pe53-pe53.

Pan, X., L.A. Kane, J.E. Van Eyk, and P.A. Coulombe. 2011. Type I keratin 17 protein is phosphorylated on serine 44 by p90 ribosomal protein S6 kinase 1 (RSK1) in a growth- and stress-dependent fashion. *Journal of Biological Chemistry* 286:42403-42413.

Pasparakis, M., I. Haase, and F.O. Nestle. 2014. Mechanisms regulating skin immunity and inflammation. *Nature reviews immunology* 14:289-301.

Pennington, K., T. Chan, M. Torres, and J. Andersen. 2018. The dynamic and stress-adaptive signaling hub of 14-3-3: emerging mechanisms of regulation and context-dependent protein–protein interactions. *Oncogene* 37:5587-5604.

Perng, Y.-C., and D.J. Lenschow. 2018. ISG15 in antiviral immunity and beyond. *Nature Reviews Microbiology* 16:423-439.

Rashmi, R., K. Rao, and K. Basavaraj. 2009. A comprehensive review of biomarkers in psoriasis. *Clinical and experimental dermatology* 34:658-663.

Rendon, A., and K. Schäkel. 2019. Psoriasis pathogenesis and treatment. *International journal of molecular sciences* 20:1475.

Renert-Yuval, Y., J.P. Thyssen, R. Bissonnette, T. Bieber, K. Kabashima, D. Hijnen, and E. Guttman-Yassky. 2021. Biomarkers in atopic dermatitis—a review on behalf of the International Eczema Council. *Journal of Allergy and Clinical Immunology* 147:1174-1190. e1171.

Ritchie, M.E., D. Diyagama, J. Neilson, R. van Laar, A. Dobrovic, A. Holloway, and G.K. Smyth. 2006. Empirical array quality weights in the analysis of microarray data. *BMC bioinformatics* 7:1-16.

Rosenblum, D., and S. Naik. 2022. Epithelial–immune crosstalk in health and disease. *Current opinion in genetics & development* 74:101910.

Sarkar, M.K., R. Uppala, C. Zeng, A.C. Billi, L.C. Tsoi, A. Kidder, X. Xing, B.E.P. White, S. Shao, and O. Plazyo. 2023. Keratinocytes sense and eliminate CRISPR DNA through

STING/IFN-κ activation and APOBEC3G induction. *The Journal of clinical investigation* 133:
Schneider, C.A., W.S. Rasband, and K.W. Eliceiri. 2012. NIH Image to ImageJ: 25 years of image analysis. *Nature methods* 9:671-675.
Seth, R.B., L. Sun, C.-K. Ea, and Z.J. Chen. 2005. Identification and characterization of MAVS, a mitochondrial antiviral signaling protein that activates NF-κB and IRF3. *Cell* 122:669-682.
Sezer, E., A. Böer-Auer, E. Cetin, F. Tokat, E. Durmaz, S. Sahin, and U. Ince. 2015. Diagnostic utility of Ki-67 and Cyclin D1 immunostaining in differentiation of psoriasis vs. other psoriasiform dermatitis. *Dermatology Practical & Conceptual* 5:7.
Smits, J.P., H. Niehues, G. Rikken, I.M. van Vlijmen-Willems, G.W. van de Zande, P.L. Zeeuwen, J. Schalkwijk, and E.H. van den Bogaard. 2017. Immortalized N/TERT keratinocytes as an alternative cell source in 3D human epidermal models. *Scientific reports* 7:11838.
Smyth, G.K. 2004. Linear models and empirical bayes methods for assessing differential expression in microarray experiments. *Statistical applications in genetics and molecular biology* 3:
Stirling, D.R., M.J. Swain-Bowden, A.M. Lucas, A.E. Carpenter, B.A. Cimini, and A. Goodman. 2021. CellProfiler 4: improvements in speed, utility and usability. *BMC bioinformatics* 22:1-11.
Sun, T., and H. Green. 1978. Keratin filaments of cultured human epidermal cells. Formation of intermolecular disulfide bonds during terminal differentiation. *Journal of Biological Chemistry* 253:2053-2060.
Swindell, W.R., K.A. Michaels, A.J. Sutter, D. Diaconu, Y. Fritz, X. Xing, M.K. Sarkar, Y. Liang, A. Tsoi, and J.E. Gudjonsson. 2017. Imiquimod has strain-dependent effects in mice and does not uniquely model human psoriasis. *Genome medicine* 9:1-21.
Szklarczyk, D., R. Kirsch, M. Koutrouli, K. Nastou, F. Mehryary, R. Hachilif, A.L. Gable, T. Fang, N.T. Doncheva, and S. Pyysalo. 2023. The STRING database in 2023: protein–protein association networks and functional enrichment analyses for any sequenced genome of interest. *Nucleic acids research* 51:D638-D646.
Thimmulappa, R.K., H. Lee, T. Rangasamy, S.P. Reddy, M. Yamamoto, T.W. Kensler, and S. Biswal. 2016. Nrf2 is a critical regulator of the innate immune response and survival during experimental sepsis. *The Journal of clinical investigation* 116:984-995.
Tilwani, S., K. Gandhi, and S.N. Dalal. 2024. 14-3-3ε conditional knockout mice exhibit defects in the development of the epidermis. *FEBS letters*
Van Der Fits, L., S. Mourits, J.S. Voerman, M. Kant, L. Boon, J.D. Laman, F. Cornelissen, A.-M. Mus, E. Florencia, and E.P. Prens. 2009. Imiquimod-induced psoriasis-like skin inflammation in mice is mediated via the IL-23/IL-17 axis. *The Journal of Immunology* 182:5836-5845.
Walter, A., M. Schäfer, V. Cecconi, C. Matter, M. Urosevic-Maiwald, B. Belloni, N. Schönewolf, R. Dummer, W. Bloch, and S. Werner. 2013. Aldara activates TLR7-independent immune defence. *Nature communications* 4:1560.
Wawersik, M., R.D. Paladini, E. Noensie, and P.A. Coulombe. 1997. A proline residue in the α-helical rod domain of type I keratin 16 destabilizes keratin heterotetramers. *Journal of Biological Chemistry* 272:32557-32565.
Weiss, G., A. Shemer, and H. Trau. 2002. The Koebner phenomenon: review of the literature. *Journal of the European Academy of Dermatology and Venereology* 16:241-248.
Xu, B., J. Musai, Y.S. Tan, G.A. Hile, W.R. Swindell, B. Klein, J.T. Qin, M.K. Sarkar, J.E. Gudjonsson, and J.M. Kahlenberg. 2024a. A critical role for IFN-β signaling for IFN-κ induction in keratinocytes. *Frontiers in Lupus* 2:1359714.

Xu, Y., E. Cohen, C.N. Johnson, C.A. Parent, and P.A. Coulombe. 2024b. Repeated stress to the skin amplifies neutrophil infiltration in a keratin 17-and PKCα-dependent manner. *Plos Biology* 22:e3002779.

Zhang, L.-j. 2019. Type1 interferons potential initiating factors linking skin wounds with psoriasis pathogenesis. *Frontiers in immunology* 10:1440.

Zhang, L.-j., G.L. Sen, N.L. Ward, A. Johnston, K. Chun, Y. Chen, C. Adase, J.A. Sanford, N. Gao, and M. Chensee. 2016. Antimicrobial peptide LL37 and MAVS signaling drive interferon-β production by epidermal keratinocytes during skin injury. *Immunity* 45:119-130.

Zhang, X., L. Lei, L. Jiang, C. Fu, J. Huang, Y. Hu, L. Zhu, F. Zhang, J. Chen, and Q. Zeng. 2023. Characteristics and pathogenesis of Koebner phenomenon. *Experimental dermatology* 32:310-323.

Zhou, R., G. Wang, D. Kim, S. Kim, N. Islam, R. Chen, Z. Wang, A. Li, E.F. McCarthy, and L. Li. 2019. dsRNA sensing induces loss of cell identity. *Journal of Investigative Dermatology* 139:91-99.

Zhu, H., F. Lou, Q. Yin, Y. Gao, Y. Sun, J. Bai, Z. Xu, Z. Liu, W. Cai, and F. Ke. 2017. RIG-I antiviral signaling drives interleukin-23 production and psoriasis-like skin disease. *EMBO molecular medicine* 9:589-604.

Zieman, A., and P. Coulombe. 2020. Pathophysiology of pachyonychia congenita-associated palmoplantar keratoderma: new insights into skin epithelial homeostasis and avenues for treatment. *British Journal of Dermatology* 182:564-573.

Zieman, A.G., B.G. Poll, J. Ma, and P.A. Coulombe. 2019. Altered keratinocyte differentiation is an early driver of keratin mutation-based palmoplantar keratoderma. *Human molecular genetics* 28:2255-2270.

Legends for main figures 1-6.

Figure 1: Keratin 16 gene expression and protein interactions are linked to Type-I interferon signaling

(A) Analysis of differential expression between *KRT16*^{high} and *KRT16*^{low} expressing cells in single-cell RNA datasets from PSOR and HS patients. Differentially expressed genes are plotted according to "% Expression in the population" (Y-axis) vs Avg Log2 fold change (X-axis). Interferon antiviral genes are highlighted in red. (B-C) Immunostaining for K16 (green) and nuclei (DAPI, blue) in tissue sections from non-lesional (B) or lesional skin (C) of individuals with psoriasis. (D) Analysis of IP/MS data from 3xflag-tagged K16 expression in HaCat keratinocytes. Highlighted are the type II keratin K6A (blue) and proteins related to interferon signaling (red). (E) Results of statistical overrepresentation analysis using Panther API (Reactome dataset). Interferon responsive genes and pathways are highlighted in red. (F) Gene network map for highest interacting proteins identified in the IP/MS that showed SAINT score >0.8. (G) Statistical overrepresentation test for differentially expressed pathways in microarray data from lesional skin of PC patients with mutations in *KRT6* or *KRT16* (source: Cao et al., 2015). (H) Statistical overrepresentation test for differentially expressed pathways in microarray data from lesional skin of *Krt16* null mice (Zieman et al., 2019).

Figure 2: *Krt16* null mice show amplified response to imiquimod model of psoriasiform disease

(A) Protocol of IMQ application used to induce psoriasiform disease in mice (see Methods). (B-E) Images of WT and *Krt16* null mice prior to treatment (day 0; B,D) and following the last treatment (day 4; C,E). Insets highlight the treated area. (F-I) H&E staining of back skin sections from WT mice (F,G) or *Krt16* null mice (H,I) treated with Vaseline control or IMQ, respectively. Images presented are maximum projection across 5um depth. (J-L) Indirect immunofluorescence for K16 (green), and K14 (red), and staining for nuclei (DAPI, blue) in back skin sections from WT mice treated with Vaseline (J) or IMQ (K), or *Krt16* null treated with IMQ (L). White dashed lines delineate the basement membrane. (M) Quantification of epidermis thickness from Vaseline- or IMQ-treated WT and *Krt16* null mice. (N-P) Indirect immunofluorescence for Ki67 (green) and K14 (red), and staining for nuclei (DAPI, blue) in back skin sections WT mice treated with Vaseline (J), IMQ (K), or *Krt16* null treated with IMQ. White dashed line delineates the basement membrane. (Q) Quantification of mitotic index (%Ki67-positive cells) from Vaseline- or IMQ-treated WT and *Krt16* null mice. (R-S') Indirect immunofluorescence for OAS1 (green), and staining of nuclei (DAPI, blue) in back skin sections following IMQ treatment of WT (R,R') and *Krt16* null mice (S-S'). Yellow boxes in (R) and (S) are shown at higher magnification in (R') and (S') . White dashed lines delineate the basement membrane, and red dashed lines depict the interface between basal and suprabasal compartments. (T) Quantification of OAS1 signal intensity (normalized from 0-1 per section) from the dermo-epidermal interface to the stratum corneum (x=0) in WT (blue) and *Krt16* null mice (red). Lines represent the mean intensity per um, with standard error across animals shown in light blue or red, respectively. One-way ANOVA with Tukey's multiple comparisons test was used to compare conditions in (M) and (Q).

Figure 3: Loss of K16 leads to increased neutrophil recruitment and OAS1 signaling after TPA treatment

(A) Protocol for TPA topical treatment of mouse ear skin (see methods). (B-D) Indirect immunofluorescence of mouse ear skin sections for neutrophil marker Ly6G (red), K16 (green), K14 (yellow), and staining for nuclei (DAPI, blue), at 6h after single TPA application to WT (B) and *Krt16* null mice (C), or dual TPA application to WT (D) or *Krt16* null ear skin (E). Dashed white lines delineate the cartilage (c) and arrow depicts dorsal to ventral direction. (F-F') Quantification of neutrophil area (F) and distribution (F') across the dermis of dorsal ear skin at 6h after single TPA treatment. (G-G') Quantification of neutrophil area (G) and distribution (G') across the dermis of dorsal ear skin at 6h after dual TPA treatments. (H-I) Indirect immunofluorescence for OAS1 (green), and staining of nuclei (DAPI, blue) in ear skin sections after dual acetone (H-H'; K-K') or dual TPA treatments (I-I'; L-L'). Yellow boxes are region of interests magnified in frames H', I', K', and L'. White dashed lines delineate the basement membrane, and red dashed lines depict the interface between basal and suprabasal compartments. (J) Quantification of OAS1 levels in ear epidermis of WT or *Krt16* null mice after dual treatment with Acetone or TPA. (M) Quantification of OAS1 signal intensity (normalized from 0-1 per section) relative to distance from the dermo-epidermal interface (x=0) in WT (blue) and *Krt16* null mice (blue). Lines represent the mean intensity per um, with standard error across animals shown in light blue or red respectively. One-way ANOVA with Tukey's multiple comparisons test was used to compare conditions in (F) and (G), and Holm-Šídák's multiple comparisons test used to compare conditions in (J).

Figure 4. PolyIC treatment of *KRT16* null NTERT keratinocytes leads to amplified production of Type I IFN targets and neutrophil recruitment

(A) Schematic depicting the mode of keratinocyte activation and downstream interferon response by dsRNA (PolyIC). (B) Western blot analysis of K16, ISG15 and p-IRF7 levels in WT and *KRT16 KO* bilayer N/TERT keratinocytes following (1) untreated, (2) polyIC treatment without recovery and (3) polyIC treatment followed by 24 hours of recovery. Presented are two biological replicates per condition (WT #1,#2; KO #1, #2). HSP90 was used as a loading control for K16 and ISG15. Cofilin was used as a loading control for p-IRF7. (C-E) Quantification of K16 (C) p-IRF7 (D) and ISG15 (E) levels across polyIC treatment conditions in WT, *KRT16* KO, or MOCK N/TERT keratinocytes. Each dot represents a biological replicate. (F-I) Indirect immunofluorescence for ISG15 (green) and staining for nuclei (DAPI, magenta) in WT (F-G) or *KRT16* KO (H-I) N/TERT keratinocytes untreated (F,H) or 24h after treatment with polyIC (G,I). (J) quantification of mean ISG15 fluorescence intensity per cell in untreated or polyIC recovered N/TERT keratinocytes. (K-N) Indirect immunofluorescence for p-IRF7 (grey) in WT (K-L) or *KRT16 KO* (M-N) N/TERT keratinocytes untreated (K,M) or 24 hours after treatment with polyIC (L,N). (O) Quantification of mean nuclear p-IRF fluorescence intensity per cell in untreated or polyIC recovered N/TERT keratinocytes. (P) Illustration depicting human neutrophil migration assay (see method). (Q) Quantification of % neutrophil migration towards conditioned media from WT (green) or *KRT16* KO (magenta) N/TERT keratinocytes, untreated or at 24h after treatment with polyIC. (R) Quantification of % neutrophil migration towards conditioned media from WT (green) or *KRT16* KO (magenta) N/TERT keratinocytes at 24 h after acetone or TPA treatment. In (Q) and (R), each dot represents a single biological replicate. One-way ANOVA with Šídák's multiple comparisons test was used to compare conditions in (C-E). Tukey multiple comparisons test was used to

compare conditions in (J) and (O). Repeated Measures one way ANOVA with Tukey's multiple comparisons test was used for statistics presented in panels (Q-R).

Figure 5. K16 binds 14-3-3epsilon, a regulator of RLR Mediated interferon activation

(A) Schematic depicting the regulation of RIG1/MDA5 and MAVS signaling by 14-3-3ε and TRIM proteins. (B) Western blot analysis of 14-3-3ε levels in WT and *KRT16 KO* bilayer N/TERT keratinocytes following (1) no treatment (control), (2) polyIC treatment and (3) at 24h after polyIC treatment. Two biological replicates per condition are reported (WT #1,#2; KO #1,#2). HSP90 was used for loading control. (C-D) Indirect immunofluorescence for K16 (green) and staining for nuclei (DAPI, blue) in the basal layer (C) and suprabasal layer (D) of post-confluent N/TERT keratinocytes. Blue rectangle in D depict the location of the magnified images in panel D'. (D'-D'') Airyscan confocal microscopy for K16 (green), 14-3-3ε (red) and nuclei (blue) in suprabasal N/TERT keratinocytes. Yellow indicates areas of colocalization between the two proteins. Yellow rectangle in D' is magnified in D''. (E-I) Proximity ligation assay (PLA) signal between K16 and 14-3-3ε (green) in basal and suprabasal layers of WT, untreated (E-F) and polyIC-treated (F-G), and of *Krt16* KO, untreated (H) and polyIC treated (I), N/TERT keratinocytes. Nuclei are stained with DAPI (grey). (J) Quantification of the K16:14-3-3ε PLA signal across N/TERT keratinocytes layers, and in *KRT16* KO controls in untreated or at 24h after polyIC treatment. (K) Immunoprecipitation of endogenous K16 from WT or *KRT16 KO* cells. Lysates and immunoprecipates fractions were blotted for K16 and 14-3-3ε. Input (2ug total) was used to validate genotype and assess for 14-3-3ε levels across conditions. K16 pulldown (IP from total 35 ug) was verified in the IP conditions, and high exposure was used to detect 14-3-3ε pulldown in the IP samples across conditions. (L) Predicted 14-3-3 binding sites in human and mouse K16. Each residue is colored by rank provided by 14-3-3 pred interface. Highlighted in red are the S44 and S40 orthologs in human and mouse, and their ranking in parentheses. (M) Illustration of approach used to generate a mass spectrometry phospho-proteomic profile of K16 following 0, 6, 12, 24 and 48 h after a single TPA treatment of ear skin in WT mice (n= 3 animals). (N) Results from MS analysis of in WT mouse ear proteins identify an increase in K16 levels across time after TPA treatment. (O) Levels of phosphorylated S40 residue in K16 across time after TPA treatment. One-way ANOVA with Tukey's multiple comparisons test was used to compare conditions in (J).

Figure 6.Loss of K16 leads to increased 14-3-3:RIG1 proximity and MAVS aggregation *ex vivo* and *in vivo.*

(A-D) Indirect immunofluorescence for RIG-I (green) and staining for nuclei (DAPI, magenta) in WT (A-B) and *KRT16* KO (C-D) N/TERT keratinocytes, either untreated (A,C) or at 24h following polyIC treatment (B,D). (E-H) PLA signal probing for close proximity between RIG-I and 14-3-3ε (green) in WT (E-F) or *KRT16* KO (G-H) N/TERT keratinocytes, either untreated (E,G) or at 24h after polyIC treatment (F,H). Nuclei were stained using DAPI (grey). (I-J') PLA signal probing for close proximity between RIG-I and 14-3-3pan (green) at 5d after IMQ treatment of mouse back skin in either WT (I, inset I') or *Krt16* null (J, inset J') mice. Yellow rectangles in I, J depict the location of the magnified image regions in I', J'. Dashed white lines depict the basement membrane. (K-L') Indirect immunofluorescence for MAVS at 5 d after IMQ treatment of mouse back skin in WT (K, inset K') and *Krt16* null (L, inset L') mice. Yellow rectangles in K, L depict the location of the magnified image regions in K',L'. Dashed white lines depict the basement membrane. (M) Quantification of RIG:14-3-3ε PLA signal in untreated and at 24h after polyIC

treatment in WT or *KRT16* KO N/TERT keratinocytes. (N) Quantification of RIG-I:14-3-3pan PLA signal in the epidermis of IMQ-treated back skin of WT or *Krt16* null mice. (O) Quantification of MAVS aggregates in epidermis of Vaseline- or IMQ-treated back skin of WT or *Krt16* null mice. One way ANOVA with Tukey's multiple comparisons test was used to compare conditions in (M), and unpaired t-test was used to compare conditions in (N) and (O).

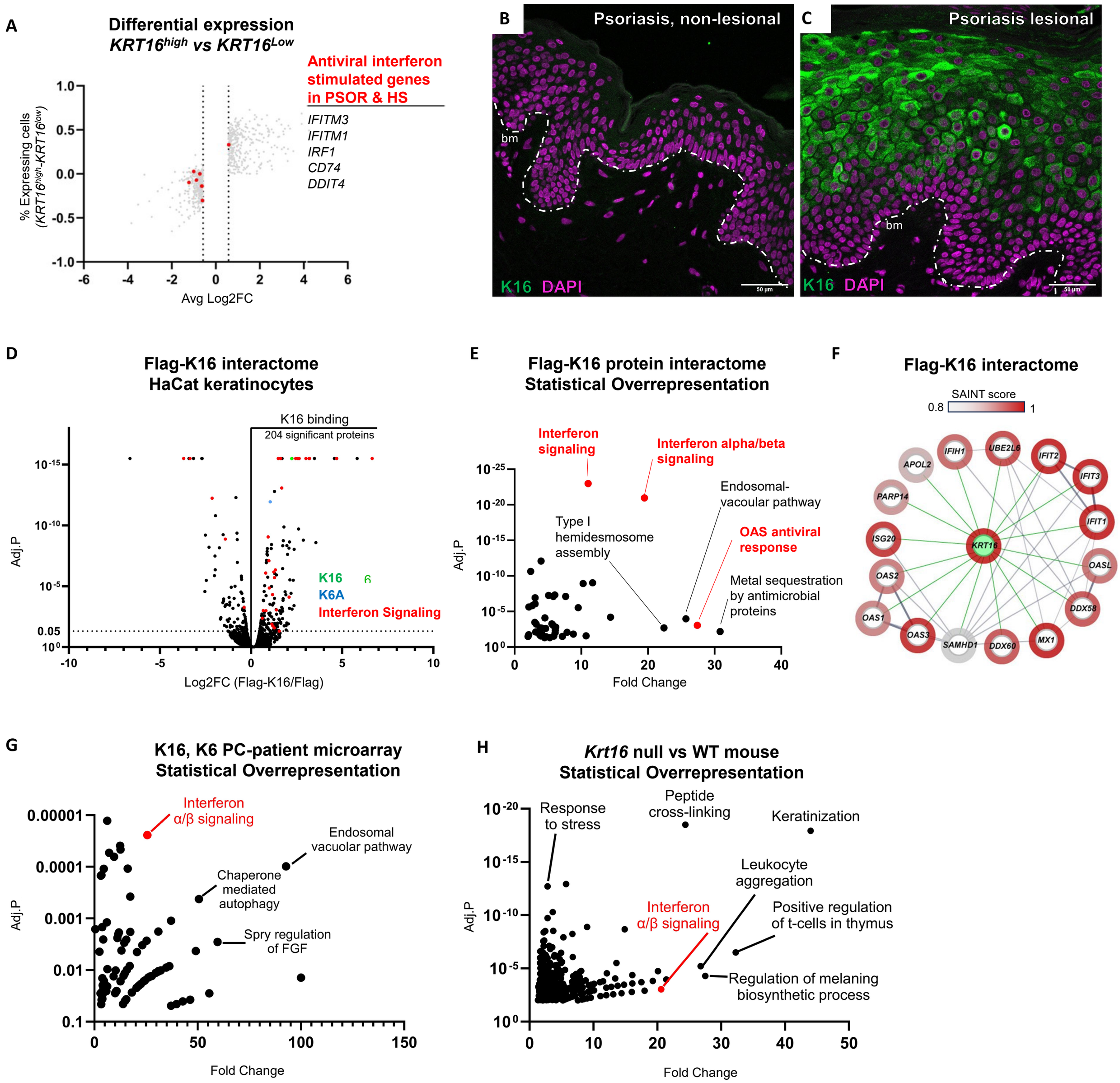
A
Differential expression
KRT16high vs KRT16Low
Antiviral interferon stimulated genes in PSOR & HS
IFITM3
IFITM1
IRF1
CD74
DDIT4
% Expressing cells (KRT16high-KRT16low)
Avg Log2FC
B
Psoriasis, non-lesional
bm
K16 DAPI
C
Psoriasis lesional
bm
K16 DAPI
D
Flag-K16 interactome
HaCat keratinocytes
K16 binding
204 significant proteins
K16
K6A
Interferon Signaling
Adj.P
Log2FC (Flag-K16/Flag)
E
Flag-K16 protein interactome
Statistical Overrepresentation
Interferon signaling
Interferon alpha/beta signaling
Endosomal-vacoular pathway
Type I hemidesmosome assembly
OAS antiviral response
Metal sequestration by antimicrobial proteins
Adj.P
Fold Change
F
Flag-K16 interactome
SAINT score
0.8
1
IFIH1
UBE2L6
IFIT2
APOL2
IFIT3
PARP14
IFIT1
ISG20
KRT16
OASL
OAS2
DDX58
OAS1
OAS3
SAMHD1
DDX60
MX1
G
K16, K6 PC-patient microarray
Statistical Overrepresentation
Interferon α/β signaling
Endosomal vacuolar pathway
Chaperone mediated autophagy
Spry regulation of FGF
Adj.P
Fold Change
H
Krt16 null vs WT mouse
Statistical Overrepresentation
Response to stress
Peptide cross-linking
Keratinization
Leukocyte aggregation
Interferon α/β signaling
Positive regulation of t-cells in thymus
Regulation of melaning biosynthetic process
Adj.P
Fold Change

Figure 1

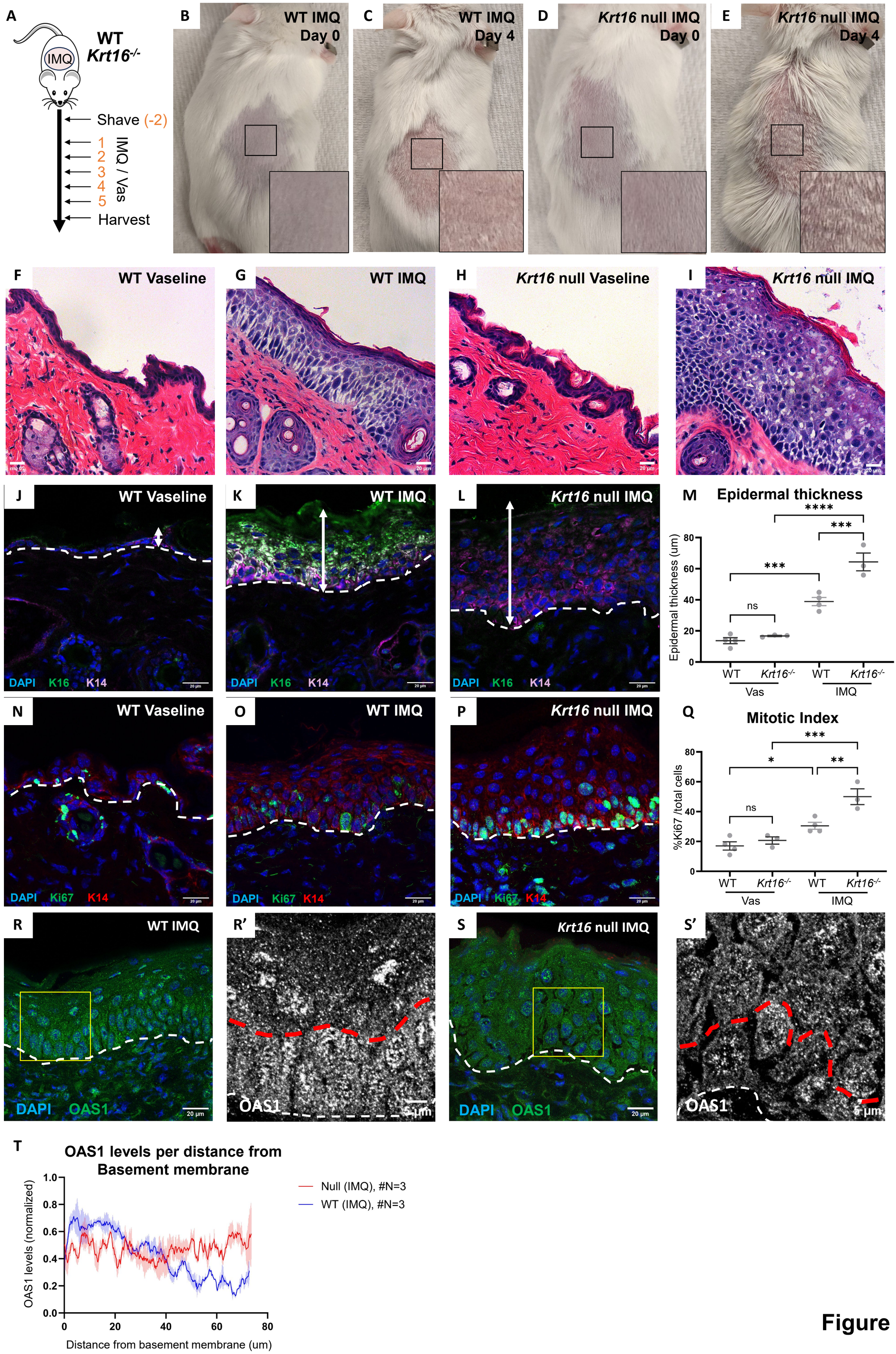
A
WT
Krt16-/-
IMQ
Shave (-2)
1
2
3
4
5
IMQ / Vas
Harvest
B WT IMQ Day 0
C WT IMQ Day 4
D Krt16 null IMQ Day 0
E Krt16 null IMQ Day 4
F WT Vaseline
G WT IMQ
H Krt16 null Vaseline
I Krt16 null IMQ
J WT Vaseline
K WT IMQ
L Krt16 null IMQ
DAPI K16 K14
M Epidermal thickness
Epidermal thickness (um)
****
***
***
ns
WT
Krt16-/-
Vas
IMQ
N WT Vaseline
O WT IMQ
P Krt16 null IMQ
DAPI Ki67 K14
Q Mitotic Index
%Ki67 /total cells
***
*
**
ns
R WT IMQ
R'
S Krt16 null IMQ
S'
DAPI OAS1
OAS1
T
OAS1 levels per distance from Basement membrane
OAS1 levels (normalized)
Distance from basement membrane (um)
Null (IMQ), #N=3
WT (IMQ), #N=3

Figure 2

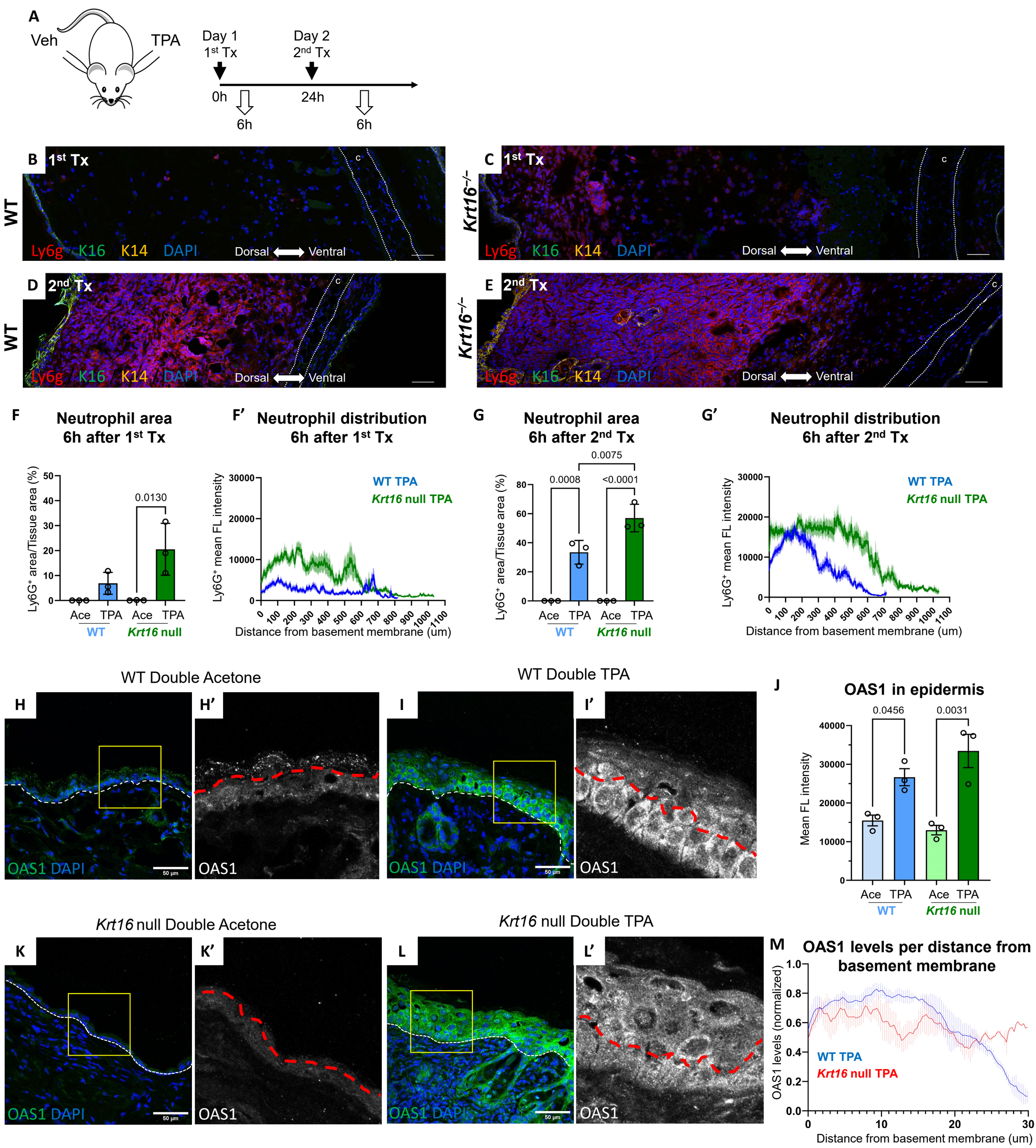
A
Veh
TPA
Day 1
1st Tx
Day 2
2nd Tx
0h
24h
6h
6h
B 1st Tx
WT
Ly6g K16 K14 DAPI
Dorsal Ventral
C 1st Tx
Krt16−/−
D 2nd Tx
E 2nd Tx
F
Neutrophil area
6h after 1st Tx
Ly6G+ area/Tissue area (%)
0.0130
Ace TPA Ace TPA
WT Krt16 null
F'
Neutrophil distribution
6h after 1st Tx
Ly6G+ mean FL intensity
WT TPA
Krt16 null TPA
Distance from basement membrane (um)
G
Neutrophil area
6h after 2nd Tx
0.0075
0.0008
<0.0001
G'
Neutrophil distribution
6h after 2nd Tx
WT Double Acetone
WT Double TPA
H
H'
I
I'
OAS1 DAPI
OAS1
50 µm
J
OAS1 in epidermis
0.0456
0.0031
Mean FL intensity
Krt16 null Double Acetone
Krt16 null Double TPA
K
K'
L
L'
M
OAS1 levels per distance from basement membrane
OAS1 levels (normalized)
Distance from basement membrane (um)

Figure 3

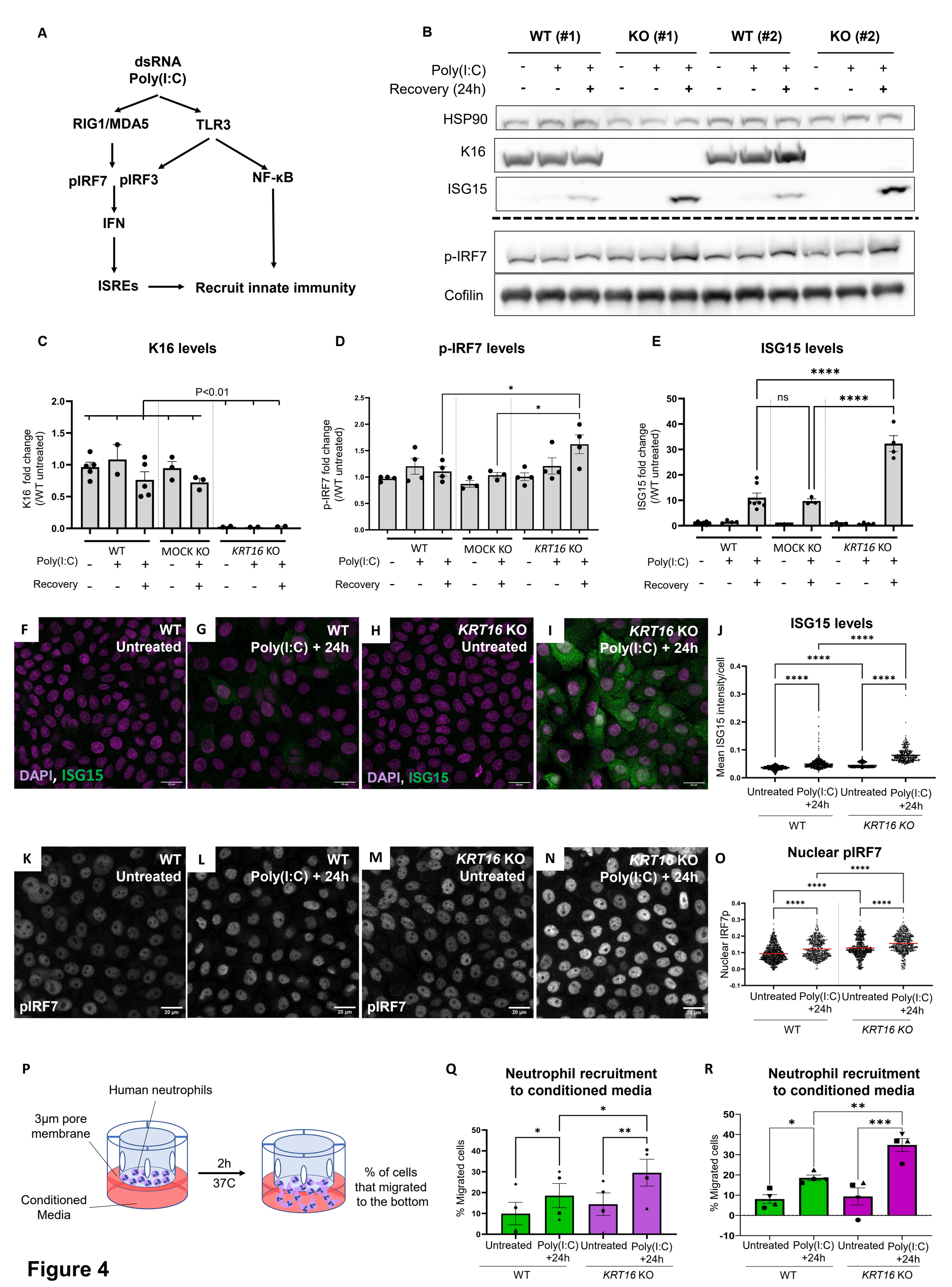
A
dsRNA
Poly(I:C)
RIG1/MDA5
TLR3
pIRF7
pIRF3
NF-κB
IFN
ISREs
Recruit innate immunity
B
WT (#1)
KO (#1)
WT (#2)
KO (#2)
Poly(I:C)
Recovery (24h)
HSP90
K16
ISG15
p-IRF7
Cofilin
C
K16 levels
P<0.01
K16 fold change (/WT untreated)
WT
MOCK KO
KRT16 KO
Poly(I:C)
Recovery
D
p-IRF7 levels
p-IRF7 fold change (/WT untreated)
E
ISG15 levels
ns
ISG15 fold change (/WT untreated)
F
WT
Untreated
DAPI, ISG15
G
WT
Poly(I:C) + 24h
H
KRT16 KO
Untreated
DAPI, ISG15
I
KRT16 KO
Poly(I:C) + 24h
J
ISG15 levels
Mean ISG15 intensity/cell
Untreated
Poly(I:C) +24h
WT
KRT16 KO
K
WT
Untreated
pIRF7
L
WT
Poly(I:C) + 24h
M
KRT16 KO
Untreated
pIRF7
N
KRT16 KO
Poly(I:C) + 24h
O
Nuclear pIRF7
Nuclear IRF7p
P
Human neutrophils
3µm pore membrane
Conditioned Media
2h
37C
% of cells that migrated to the bottom
Q
Neutrophil recruitment to conditioned media
% Migrated cells
R
Neutrophil recruitment to conditioned media
% Migrated cells

Figure 4

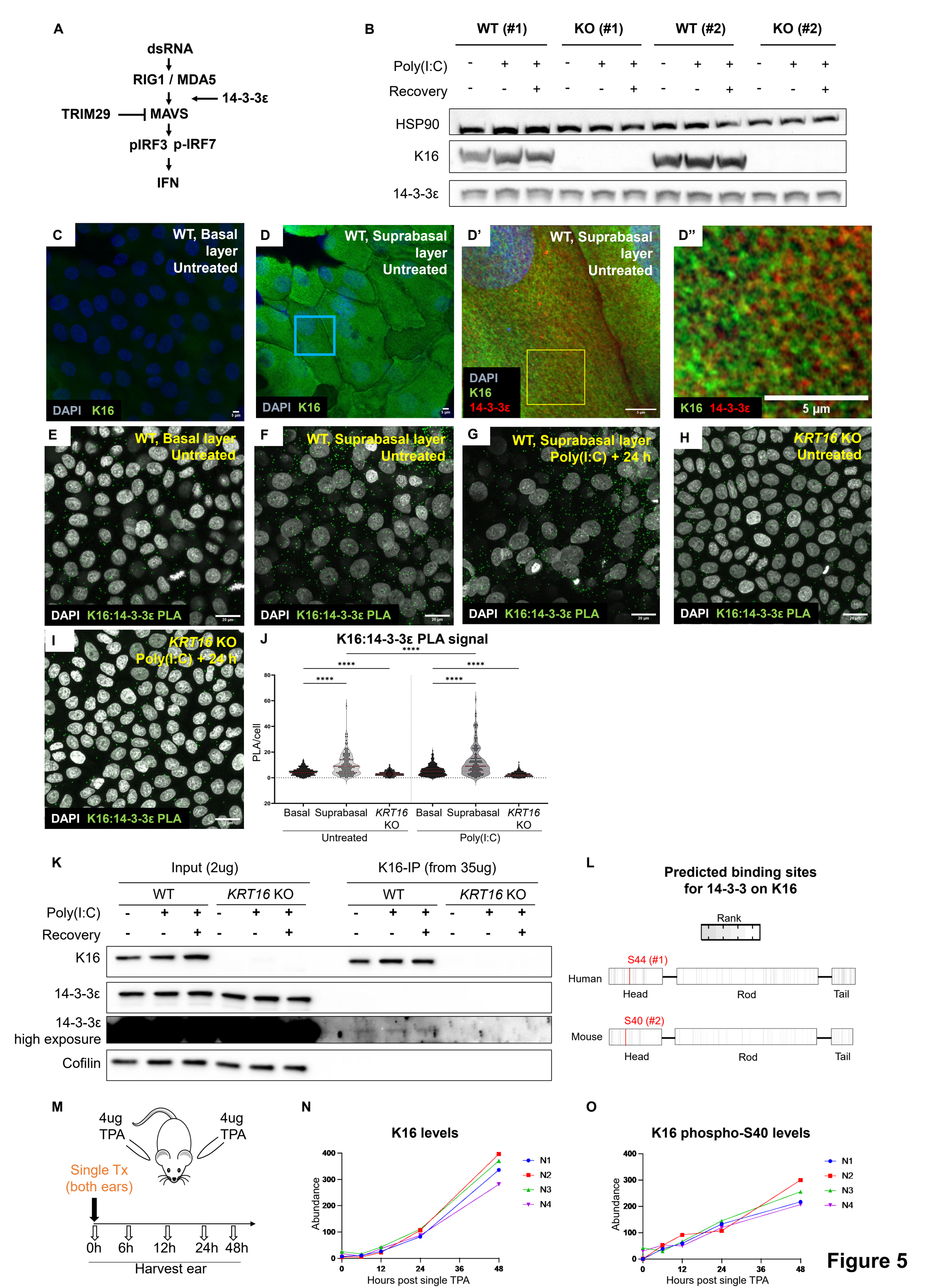
A
dsRNA
RIG1 / MDA5
14-3-3ε
TRIM29
MAVS
pIRF3 p-IRF7
IFN
B
WT (#1)
KO (#1)
WT (#2)
KO (#2)
Poly(I:C)
Recovery
HSP90
K16
14-3-3ε
C
WT, Basal layer Untreated
DAPI K16
D
WT, Suprabasal layer Untreated
DAPI K16
D'
WT, Suprabasal layer Untreated
DAPI K16 14-3-3ε
D''
K16 14-3-3ε
5 µm
E
WT, Basal layer Untreated
DAPI K16:14-3-3ε PLA
F
WT, Suprabasal layer Untreated
DAPI K16:14-3-3ε PLA
G
WT, Suprabasal layer Poly(I:C) + 24 h
DAPI K16:14-3-3ε PLA
H
KRT16 KO Untreated
DAPI K16:14-3-3ε PLA
I
KRT16 KO Poly(I:C) + 24 h
DAPI K16:14-3-3ε PLA
J
K16:14-3-3ε PLA signal
PLA/cell
Basal
Suprabasal
KRT16 KO
Untreated
Poly(I:C)
K
Input (2ug)
K16-IP (from 35ug)
WT
KRT16 KO
Poly(I:C)
Recovery
K16
14-3-3ε
14-3-3ε high exposure
Cofilin
L
Predicted binding sites for 14-3-3 on K16
Rank
S44 (#1)
Human
Head
Rod
Tail
S40 (#2)
Mouse
M
4ug TPA
Single Tx (both ears)
0h
6h
12h
24h
48h
Harvest ear
N
K16 levels
Abundance
Hours post single TPA
N1
N2
N3
N4
O
K16 phospho-S40 levels
Abundance
Hours post single TPA
N1
N2
N3
N4

Figure 5

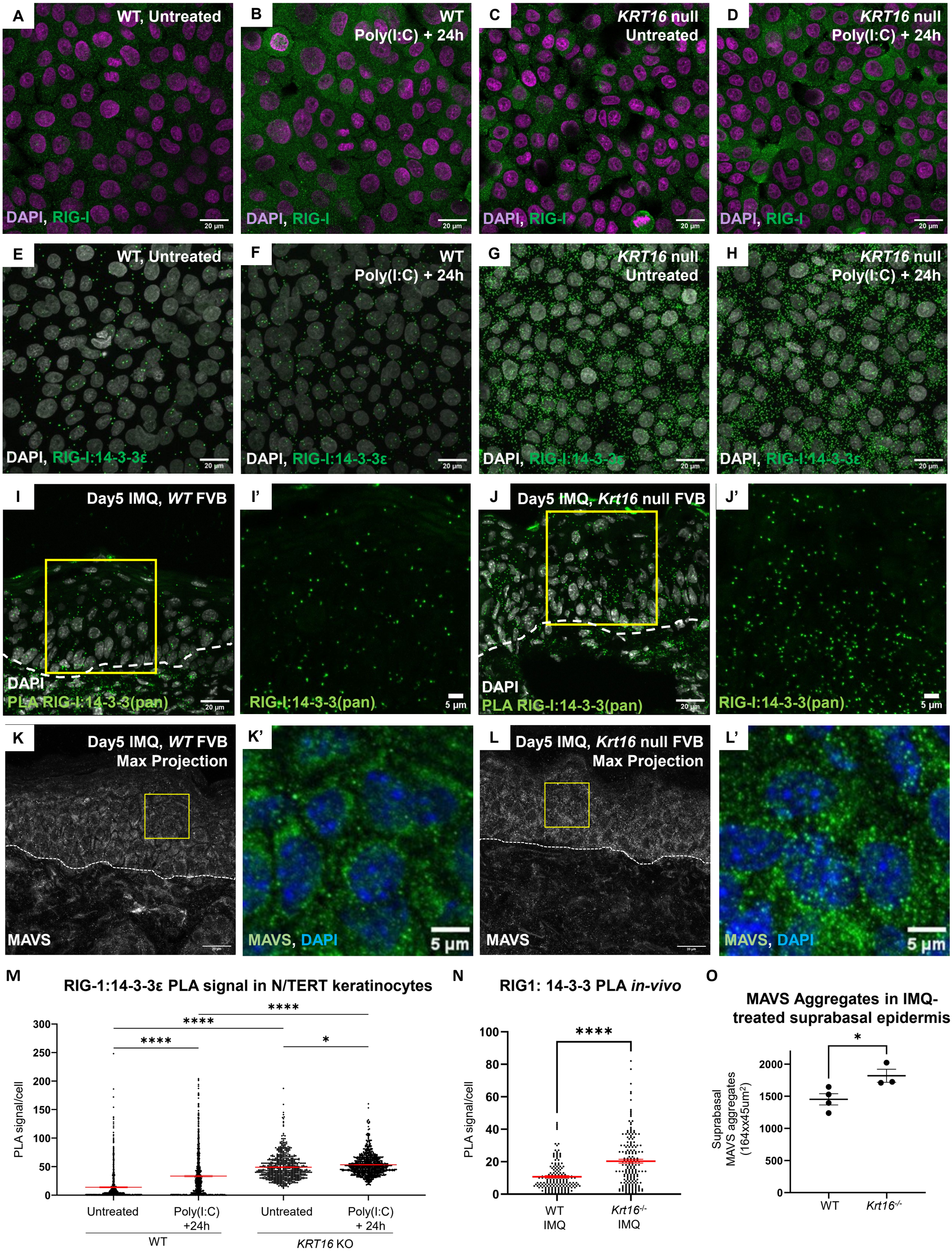
A
WT, Untreated
DAPI, RIG-I
20 µm
B
WT
Poly(I:C) + 24h
DAPI, RIG-I
20 µm
C
KRT16 null
Untreated
DAPI, RIG-I
20 µm
D
KRT16 null
Poly(I:C) + 24h
DAPI, RIG-I
20 µm
E
WT, Untreated
DAPI, RIG-I:14-3-3ε
20 µm
F
WT
Poly(I:C) + 24h
DAPI, RIG-I:14-3-3ε
20 µm
G
KRT16 null
Untreated
DAPI, RIG-I:14-3-3ε
20 µm
H
KRT16 null
Poly(I:C) + 24h
DAPI, RIG-I:14-3-3ε
20 µm
I
Day5 IMQ, WT FVB
DAPI
PLA RIG-I:14-3-3(pan)
20 µm
I'
RIG-I:14-3-3(pan)
5 µm
J
Day5 IMQ, Krt16 null FVB
DAPI
PLA RIG-I:14-3-3(pan)
20 µm
J'
RIG-I:14-3-3(pan)
5 µm
K
Day5 IMQ, WT FVB
Max Projection
MAVS
K'
MAVS, DAPI
5 µm
L
Day5 IMQ, Krt16 null FVB
Max Projection
MAVS
L'
MAVS, DAPI
5 µm
M
RIG-1:14-3-3ε PLA signal in N/TERT keratinocytes
PLA signal/cell
300
250
200
150
100
50
0
****
****
****
*
Untreated
Poly(I:C) +24h
Untreated
Poly(I:C) + 24h
WT
KRT16 KO
N
RIG1: 14-3-3 PLA in-vivo
PLA signal/cell
100
80
60
40
20
0
****
WT IMQ
Krt16-/- IMQ
O
MAVS Aggregates in IMQ-treated suprabasal epidermis
Suprabasal MAVS aggregates (164xx45um2)
2000
1500
1000
500
0
*
WT
Krt16-/-

Figure 6